FISEVIER

Contents lists available at ScienceDirect

Palaeogeography, Palaeoclimatology, Palaeoecology

journal homepage: www.elsevier.com/locate/palaeo



Invited Research Article

An algorithm-guided Ediacaran global composite $\delta^{13} C_{carb}\text{--Bayesian}$ age model

Cedric J. Hagen a,b,*, Jessica R. Creveling a

- ^a College of Earth, Ocean, and Atmospheric Sciences, Oregon State University, Corvallis, OR, USA
- ^b Department of Geological Sciences, University of Colorado Boulder, Boulder, CO, USA

ARTICLE INFO

Editor: H Falcon-Lang

Keywords:
Neoproterozoic
Shuram carbon-isotope excursion
Gaskiers glaciation
stratigraphic correlation
dynamic time warping
chemostratigraphy

ABSTRACT

While it remains uncertain whether excursions in the stable carbon isotopic composition of Ediacaran marine carbonate (813Ccarb) represent globally synchronous events (or a direct measure of ocean carbon cycling), the absence of widely distributed and readily preservable fauna, and the presence of several iconic carbon isotope excursions (CIEs), has sustained $\delta^{13}C_{carb}$ correlation as the primary means to establish relative time relationships for Ediacaran successions. Here we present an Ediacaran global $\delta^{13}C_{carb}$ composite built with a dynamic time warping (DTW) time-normalization algorithm that generates libraries of least-squares alignments between chemostratigraphic records of unequal length and distinct sediment accumulation rates. When developing a $\delta^{13}C_{carb}$ composite for each of 16 globally distributed Ediacaran paleo-depositional regions, we selected high Pearson r alignments that conformed with published geological guidance about the correlation of constituent sections. When applying DTW to align these regional algorithmic composites into one global $\delta^{13}C_{carb}$ stack, we selected alignments that allied the excursions that field workers have established (or speculated) are the Marinoan cap carbonate excursion, the Shuram excursion, and/or the basal Cambrian excursion. There are strengths and weaknesses to making explicit the temporal relationships (point-to-point correspondences) often left implicit in visual correlation. One strength is to extrapolate depositional ages by means of isotopic correlation, and here we explored this with a Bayesian Markov chain Monte Carlo age model that predicts a median age, and uncertainty, for every carbonate stratum in the global Ediacaran $\delta^{13}C_{carb}$ composite. Yet, one must caution against a false accuracy that can arise from selecting one alignment among many possibilities—the likelihood that timeuncertain time series can be stretched and squeezed into one unequivocal alignment is low. Thus, while these alignments are grounded in the expert assessment of the field worker, this global Ediacaran $\delta^{13}C_{carb}$ -Bayesian age model should be viewed as a working hypothesis to enrich, but not arbitrate, discussions of the correlation, synchrony, and completeness of Ediacaran successions.

1. Introduction

The Ediacaran Period (\sim 635–538.8 \pm 0.2 Ma; Cohen et al., 2013; Knoll et al., 2006) was a singularly dynamic interval of Earth history bracketed by the long-lived Cryogenian global glaciations (Hoffman et al., 1998; Kirschvink, 1992) and the Cambrian "Explosion" of animals (Erwin et al., 2011; Maloof et al., 2010a; Marshall, 2006). Ediacaran rocks record the diversification of both micro- and macrofossil eukaryotes (Narbonne et al., 2012; Porter, 2004), most notably the Ediacaran fauna (Droser and Gehling, 2015; Morris, 1993; Narbonne, 2005; Yuan et al., 2011); large amplitude excursions in the stable carbon isotope composition of marine carbonate (δ^{13} C_{carb}; Halverson et al., 2005;

Johnston et al., 2012; Macdonald et al., 2013), including the Shuram excursion (Bergmann et al., 2011; Burns and Matter, 1993; Busch et al., 2022; Corsetti and Kaufman, 2003; Cui et al., 2017; Fike et al., 2006; Grotzinger et al., 2011; Husson et al., 2015); the fleeting Gaskiers glaciation (Hoffman and Li, 2009; Pu et al., 2016), or a geographically and temporally more extensive ice age (Wang et al., 2023); and marine redox heterogeneity across space and time (Chen et al., 2015; Li et al., 2015; Osburn et al., 2015; Sahoo et al., 2016; Sperling et al., 2015).

All outstanding questions about Ediacaran geobiological, biogeochemical, and paleoclimatological events—and their purported causal relationships—benefit from a robust global chronology (Knoll et al., 2006; Xiao et al., 2016). For example, refined rates of Shuram excursion

^{*} Corresponding author at: Department of Geological Sciences, University of Colorado Boulder, Boulder, CO, USA. *E-mail address*: Cedric.Hagen@Colorado.edu (C.J. Hagen).

isotopic depletion (574.0 \pm 4.7–567.3 \pm 3.0 Ma; Rooney et al., 2020) may inform estimates of oxidant demand in Ediacaran oceans and atmosphere (e.g., Bristow and Kennedy, 2008; Bjerrum and Canfield, 2011; Derry, 2010; Fike et al., 2006; Paulsen et al., 2017; Rothman et al., 2003; Schrag et al., 2013; Shields et al., 2019; Busch et al., 2022). A refined chronology could clarify the synchrony or asynchrony of Ediacaran glacial deposits, and indicate whether non-glacial strata accumulated within the narrow time bounds for the Gaskiers glaciation sensu stricto, thereby resolving the geographic scope of Ediacaran glacial advance(s) (Pu et al., 2016; Wang et al., 2023). While absolute ages for Ediacaran events have expanded dramatically, they remain restricted in time and space. Most ages cluster around the Marinoan deglaciation (Condon et al., 2005; Rooney et al., 2015; Prave et al., 2016), the Gaskiers glaciation sensu stricto in Avalonia (Pu et al., 2016), the Shuram excursion (Rooney et al., 2020), and the Ediacaran-Cambrian transition (Bowring et al., 2007; Linnemann et al., 2019; Nelson et al.,

2022), leaving much of Ediacaran time poorly constrained. Moreover, Ediacaran radioisotopic ages intercalated in marine carbonate successions occur in only a limited number of paleo-geographic regions (Yang et al., 2021).

The correlation and alignment of stable carbon isotope records of marine carbonate ($\delta^{13}C_{carb}$) is a long-standing tool to unite local relative chronologies into a global framework (Halverson et al., 2005; Kaufman and Knoll, 1995; Knoll et al., 1986; Saltzman, 2005; Scholle and Arthur, 1980). The correlation of records is enabled, in part, by the assumption that excursions in $\delta^{13}C_{carb}$ are globally synchronous and affect all carbonates produced at a particular time. This assumption has come under justified scrutiny, yet the statement that Ediacaran Period carbon isotope excursions (CIEs) seem to be synchronous within the uncertainty of the radiometric dating techniques appears broadly true (Rooney et al., 2020), though important details remain to be worked out (Yang et al., 2021). Despite this substantial caveat, the absence of widely distributed

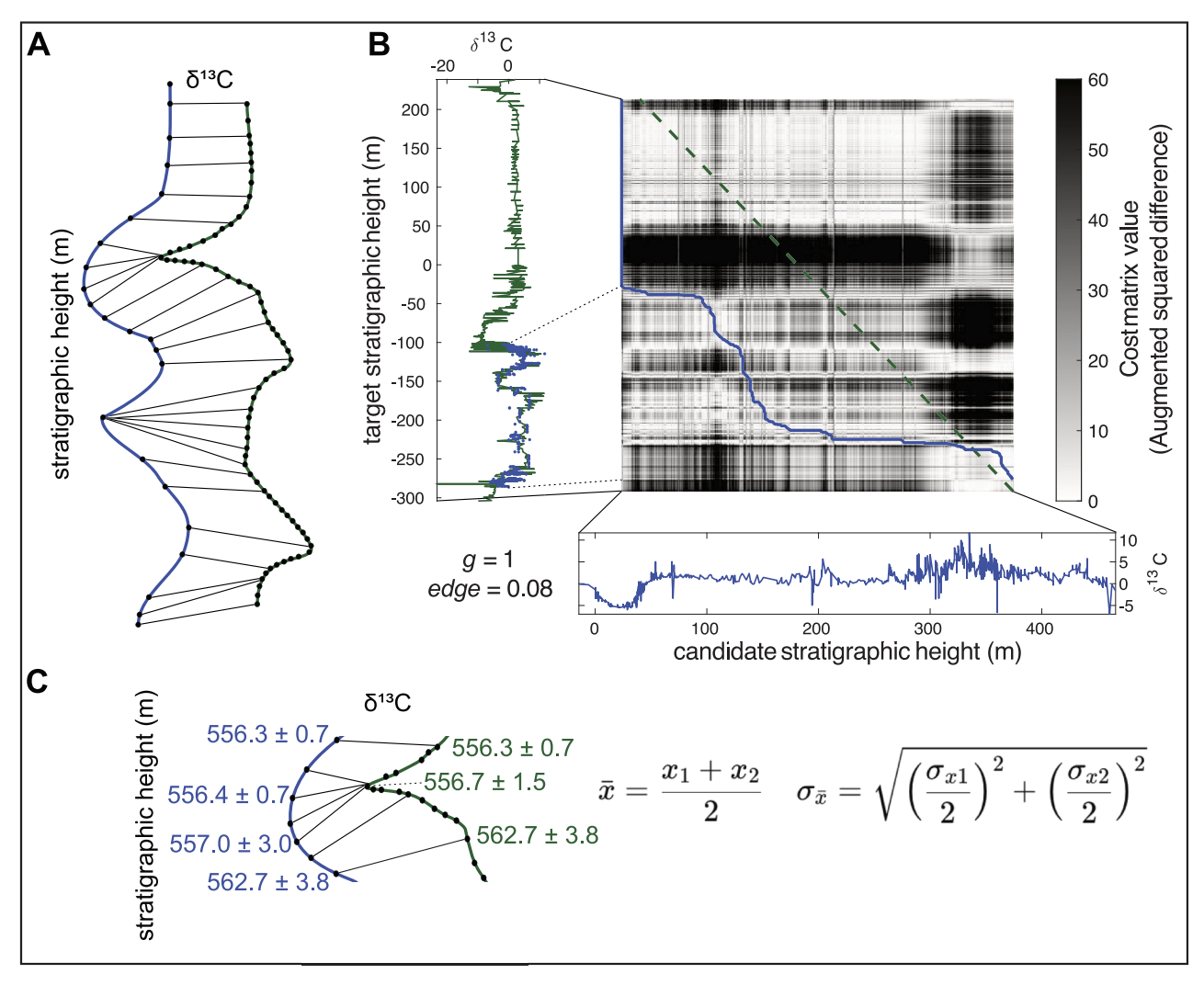


Fig. 1. A demonstration of DTW alignment of a candidate and target $\delta^{13}C_{carb}$ timeseries. A, an illustration demonstrating how dynamic time warping 'warps' timeseries records together, identifying a mathematically optimal fit by stretching and/or squeezing portions of the candidate record relative to the target record. B, a candidate chemostratigraphic record shown both unaligned (horizontally along the bottom of the figure, in blue) and aligned to a target record is shown (blue dots in the left panel overlain on the green target stratigraphic record). The center of the figure shows the augmented cost matrix, colored according to the cost matrix value (augmented squared difference). The blue line depicts the alignment path through the cost matrix corresponding with the candidate-target alignment shown in the left panel. The dashed green line indicates where the candidate stratigraphic record height is equal to the target stratigraphic record height, indicating equal accumulation rates. Horizontal segments of the alignment path indicate a condensed target record, while vertical segments indicate a condensed candidate record (except the initial vertical line along the right edge of the cost matrix, which indicates where the candidate–target alignment path 'enters' the cost matrix and corresponds to where the uppermost $\delta^{13}C_{carb}$ value of the candidate record is aligned in the target record). In this example (g = 1.00; edge = 0.08), data from Ediacaran records in northern Namibia were used as the candidate record (blue) and data from Ediacaran records in China were used as the target record (green). C, a demonstration of how age model construction is handled when multiple age constraints are assigned to the same stratigraphic height in the time-calibrated composite: we assign the horizon the mean age (\bar{x}) with the corresponding uncertainty ($\sigma_{\bar{x}}$) computed in quadrature.

and readily preservable fauna, and the presence of several iconic CIEs, have compelled many to apply $\delta^{13}C_{carb}$ chemostratigraphic correlation to establish the relative time relationships for worldwide Ediacaran stratigraphic successions (Bold et al., 2016; Bowyer et al., 2021; Halverson et al., 2005; Macdonald et al., 2013; Rooney et al., 2020; Yang et al., 2021; Zhang et al., 2022).

Here we continue this tradition by presenting the first global Ediacaran $\delta^{13}C_{carb}$ composite built with a dynamic time warping (DTW) algorithm (Hagen et al., 2024; Hay et al., 2019). This algorithmic approach generates a library of least-squares alignments between two chemostratigraphic records of unequal length and unique sediment accumulation rates. From each library we selected a single alignment

consistent with the correlation proposed by primary field workers; in this manner we aimed to synergize the point-to-point alignment of sequences afforded by an algorithm and the expertise of the field geologist. Further, we conditioned a Bayesian Markov chain Monte Carlo (B-McMC) age model on the high-precision ages intercalated within these marine carbonate successions. Together, these tools produced a probabilistic age model (mean and uncertainty) for every $\delta^{13}C_{\text{carb}}$ value in the algorithmic compilation. This output serves as one working hypothesis for the chronostratigraphy of globally distributed Ediacaran shallow-marine records; we hope that iterative refinement of the correlation of individual basins considered herein, and added subsequently, will continue to generate age models that resolve the outstanding questions

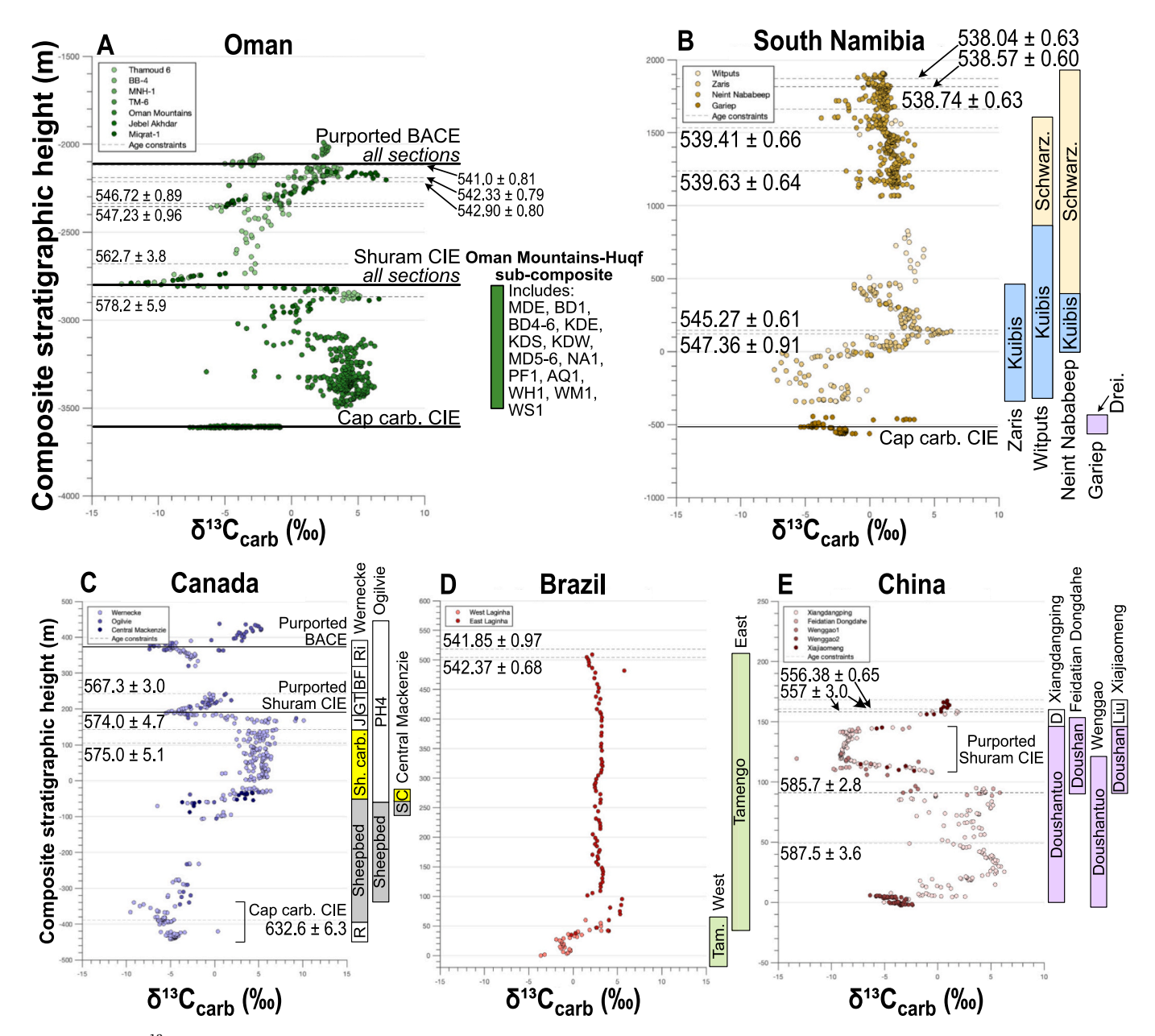


Fig. 2. The DTW $\delta^{13}C_{carb}$ composites for five Ediacaran regions with geochronologic constraints (Oman, South Namibia, Canada, Brazil, China). Each aligned record is color-coded gradationally according to the legend and region (Oman in A; South Namibia in B; Canada in C; Brazil in D; China in E. Geochronologic age constraints are shown as black dashed lines (see Table 2). Stratigraphic formations are shown on the right. Refer to Table 1 and text for details on composite construction. BACE refers to the basal Cambrian carbon isotope excursion, CIE is an abbreviation for carbon isotope excursion, and Cap carb. is an abbreviation for cap carbonate unit, D is Dengying Formation, Doushan is Doushantuo Formation, Liu is Liuchapo Formation, R is Ravensthroat Formation, Sh. carb. and C are Sheepbed carbonate, J is June Beds, GT is Gametrail Formation, BF is Blueflower Formation, Ri is Risky Formation, S is Sheepbed Formation, Schwarz. is Schwarzrand Supergroup, Drei. is Dreigratberg member, and Tam. is Tamengo Formation.

of Ediacaran earth history.

2. Methodology, assumptions, and limitations

We took the following steps to produce a global Ediacaran δ¹³C_{carb}-Bayesian age model. First, we applied dynamic time warping (Section 2.1; Fig. 1) to construct $\delta^{13}C_{carb}$ composites for 16 Ediacaran paleo-depositional regions (Section 2.2; Figs. 2-4; Table 1). For each paleo-depositional region (herein 'region'), we selected alignments that were consistent with published correlations informed by geological observation, as described in Table 1. Second, we applied DTW to align the five regional $\delta^{13}C_{carb}$ composites with radioisotopic depositional ages (Section 2.3; Fig. 5; Tables 2 and 3). The chosen interbasinal alignments chronologically sequenced these ages while also aligning the CIEs that primary field workers had identified as (or speculated were) the basal Marinoan cap carbonate CIE, the Shuram/Wonoka CIE and/or a CIE consistent with the basal Cambrian excursion (BACE). Third, we conditioned a Bayesian Markov chain Monte Carlo (B-McMC) age model on 25 radioisotopic ages intercalated within this selection of chemostratigraphic sections to generate an Ediacaran 'δ¹³C_{carb}–Bayesian age model backbone' (Section 2.3; Fig. 5). Finally, we again leveraged DTW to align the 11 temporally unconstrained regional $\delta^{13}C_{carb}$ composites to this age-model backbone to complete the global Ediacaran δ¹³C_{carb}-Bayesian age model presented here (Section 2.4; Fig. 6; Table 3). This global Ediacaran $\delta^{13}C_{carb}$ -B-McMC age model yields a probabilistic age for every $\delta^{13}C_{carb}$ value in the compilation, thus yielding a permissible high-resolution chronostratigraphic framework for global Ediacaran shallow-marine carbonate successions.

2.1. Dynamic time warping as a tool for chemostratigraphic correlation

Dynamic time warping is a ubiquitous algorithmic approach to align time series of different duration and speed (Sakoe and Chiba, 1978). As such, DTW is an ideal method to align $\delta^{13}C_{\text{carb}}$ chemostratigraphic records which overlap, yet may be offset in time, and have distortions and gaps from variable accumulation rates and sampling densities (Fig. 1a; Haam and Huybers, 2010; Hay et al., 2019; Lisiecki and Lisiecki, 2002; Lisiecki and Raymo, 2005). Each DTW alignment requires the designation of a 'target' record of relatively high data density that provides the scaffold onto which the algorithm aligns the less complete 'candidate' record. The aligned candidate record is presented on the target record's height/depth axis. A target record can be an individual (unwarped) chemostratigraphic record or a composite of previously aligned records. Here we apply the term "record" to an individual $\delta^{13}C_{\text{carb}}$ sequence and the term "composite" to a stack of multiple records, irrespective of the stacking method (algorithmic or visual).

DTW employs a least-squares optimization, under certain restrictions, to align two time series. The algorithm constructs an n by mcost matrix (C) of all possible pairings of the $\delta^{13}C_{carb}$ values from two chemostratigraphic records. Each matrix element is computed as the squared difference between a value in the target (x_n) and the candidate sequence (y_m) : $C(n,m) = (x_n - y_m)^2$. An algorithmic alignment takes the form of a warping path p through the cost matrix that minimizes the sum of squares as it assigns each index m from the candidate sequence to an index n of the target sequence. The warping path responds to two stratigraphically meaningful restrictions (penalties) applied to the cost matrix (Fig. 1b; Sakoe and Chiba, 1978; Hagen et al., 2024). The edge parameter explores whether two records span the same total interval of time by penalizing (applying an additional cost to) data in the candidate record that fall outside the time span of the target record. Higher edge values encourage overlap between the two records, whereas lower values allow the top and/or base of the candidate to extend beyond the target record. The g parameter explores similarity in accumulation rates during the shared interval of deposition by penalizing the insertion of hiatuses (i.e., adding a cost to many-to-one and one-to-many point assignments). Values of g < 1 encourage stretching or squeezing, and

values of g > 1 encourage similar rates. Because the temporal overlap and relative accumulation rate between the target and candidate records are unknown, the systematic exploration of edge and g parameter spaces generates a library of alignment solutions (Hay et al., 2019). Here we adopt the algorithm and alignment procedure of Hay et al. (2019) which generates a library of 60 alignments for each target–candidate pair, equal to the gradation of edge (0.01–0.15) and g (0.98–1.01) in increments of 0.01. For more detail, see Hagen et al. (2024).

By design, each DTW alignment is achieved by assigning single *and* multiple points in one time series to a single point in the other time series (Fig. 1a). In physical terms, each many-to-one point assignment imposes a hiatus that dynamically stretches/squeezes the height/time axis, hence the colloquialism 'dynamic time warping'. Here hiatus is used to mean an interruption, or pause, in time continuity without specifying causality; this time interruption is *relative to* the continuity of the other record. These imposed hiatuses may reflect finite chemostratigraphic sampling or other reasons. In Section 2.3.2 we discuss the implications of many–to–one point assignments for the Bayesian age model.

Every $\delta^{13}C_{carb}$ correlation, whether visual or algorithmic, rests upon the assumption that CIEs are synchronous. However, visual conjectures of temporal correspondence differ from least-squares optimizations of individual isotopic values. In principle, the DTW approach affords an unprecedented exploration of the relative time relationships between worldwide Ediacaran stratigraphic successions; in practice, the resulting geochronological hypotheses for correlation rest on consequential and unaffirmed assumptions that: (1) CIEs are globally synchronous, (2) that the preserved $\delta^{13}C_{carb}$ values record, in some manner, global seawater composition (enable point-to-point alignment), and (3) that the chosen algorithmic alignment is accurate. While our composites incorporate those stratigraphic sections for which primary field workers made compelling arguments for intra- and interbasinal correlation, the resulting Ediacaran $\delta^{13}C_{carb}$ –B-McMC age model should be viewed as a working hypothesis open to scrutiny and refinement.

Where primary workers have proposed the correlation of records with $\delta^{13}C_{carb}$ isotopic gradients across platform depth (cf. Jiang et al., 2007), we employed an alternative formulation of DTW that normalizes each record to have the same mean and variance such that the magnitude of a primary signal is not a constraint on the alignment. To achieve this, we subtracted the mean $\delta^{13}C_{carb}$ value from every data point in the record and divided differences by the standard deviation of the sequence following Hay et al. (2019). Normalized alignments are noted by asterisks in Table 1.

2.2. Constructing Ediacaran regional $\delta^{13}C_{carb}$ composites with a dynamic time warping algorithm

To develop $\delta^{13}C_{carb}$ composites for the 16 paleo-depositional regions (Table 1, column A), we assembled $\delta^{13}C_{carb}$ chemostratigraphic records from English-language publications and culled these to include those records with roughly meter-scale or finer sampling resolution and at least $\sim\!20\,\delta^{13}C_{carb}$ values (Table 1, columns B and C). The latter criterion excludes short $\delta^{13}C_{carb}$ sequences that yield multiple alignments that cannot be differentiated by geology. Based upon these criteria we opted not to develop a $\delta^{13}C_{carb}$ composite for the Sierras Bayas Group, Argentina (Bagnoud-Velásquez et al., 2013); the Volta Basin, West Africa (Porter et al., 2004); or the Avalon zone, southeast Newfoundland (Narbonne and Gehling, 2003).

We leaned upon the geological wisdom embedded within published $\delta^{13}C_{carb}$ correlations for each paleo-depositional region to choose which one of the 60 algorithmic alignments from the alignment library would contribute to a given composite (Table 1, column D). These previously published correlations are reproduced in the Supplementary File (Figs. S2–S53). For every DTW target–candidate alignment library, we selected the highest Pearson correlation coefficient (r) alignment that broadly conformed to the primary field geologist's chemostratigraphic correlation. In many circumstances the alignment with the highest

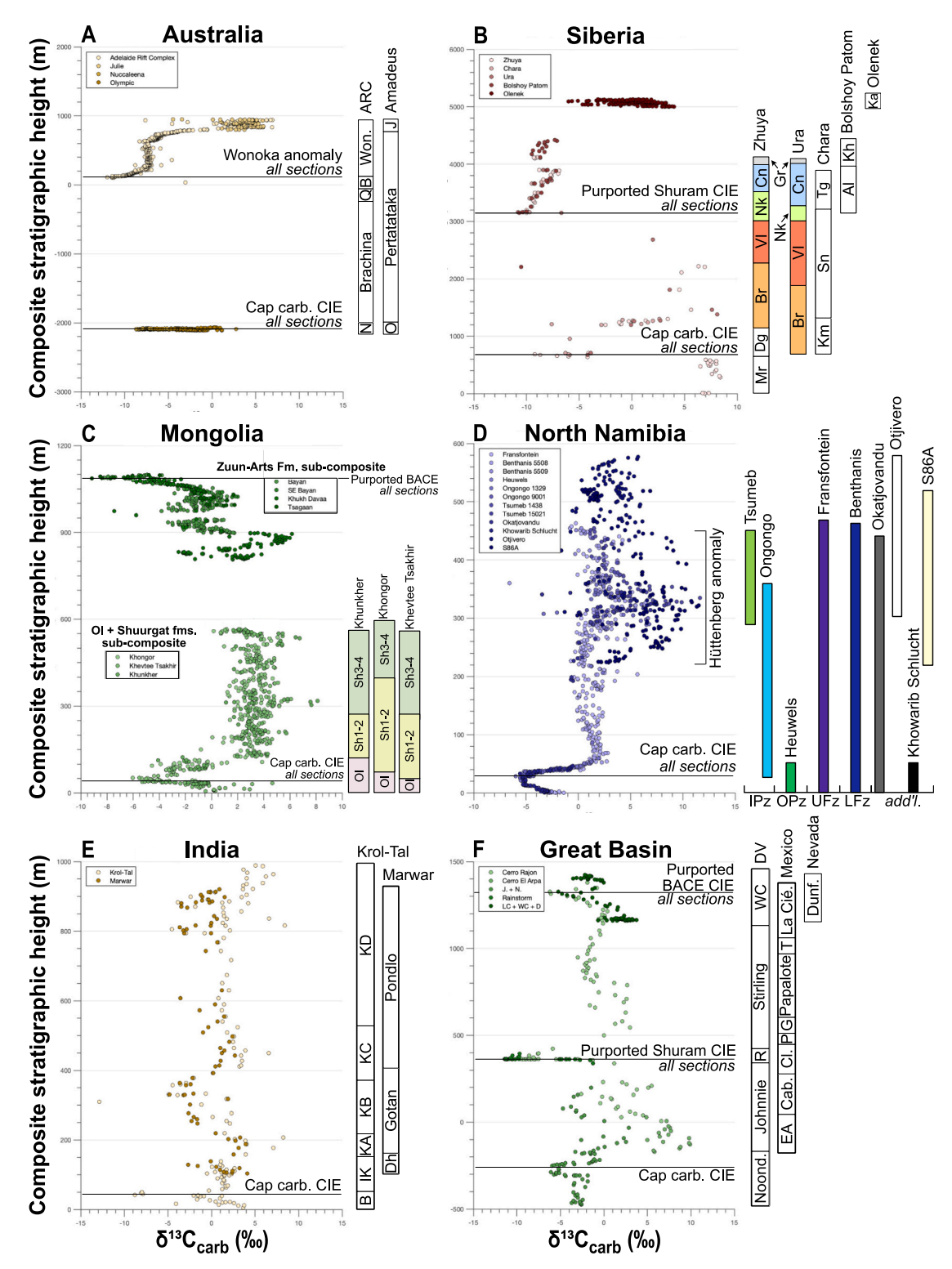


Fig. 3. The DTW $\delta^{13}C_{carb}$ composites for regions with high-resolution $\delta^{13}C_{carb}$ records but without geochronologic constraints (Australia, Siberia, Mongolia, North Namibia, India, and Great Basin). Each aligned record is color-coded gradationally according to the legend and region (Australia in A; Siberia in B; Mongolia in C; North Namibia in D; India in E; Great Basin in F). Stratigraphic formations are shown on the right. Refer to Table 1 and text for details on composite construction. Abbreviations as in Fig. 2, and N is Nuccaleena Formation, Q is ABC quartzite, B is Bunyeroo Gorge Formation, Won. is Wonoka Formation, O is Olympic Formation, J is Julie Formation, Noond. is Noonday Formation, R is Rainstorm member, WC is Wood Canyon Formation, EA is El Arpa Formation, Cab. is Caborca Formation, Cl. is Clemente Formation, P is Pitiquito Quartzite, G is Gamuza Formation, T is Tecolote Quartzite, La Cié. is La Ciénega Formation, Dunf. is Dunfee Formation, B is Blaini Formation, IK is Intra Krol Formation, KA is Krol A, KB is Krol B, KC is Krol C, KD is Krol D, Dh is Dhanapa Dolomite, Sh is the Shuurgat Formation, Mr. is Mariinsk Formation, Dg is Dzhemkukan Formation, Br is Barakun Formation, VI is Balyukhta Formation, Nk is Nikol'skoe Formation, Cn is Chencha Formation, Gr is Zherba Formation, Km is Kumukulakh Formation, Sn is Imalyk Formation, Tg is Torgo Formation, Al is Alyanchskaya Formation, Kh is Kholychskaya Formation, and Ka is Khatyspyt Formation, and IPz is Inner platform, OPz is Outer platform, UFz is Upper Foreslope, and LFz is Lower Foreslope. Depositional environment interpretations (IPz, OPz, UFz, and LFz) adopted from Hoffman and Lamothe (2019).

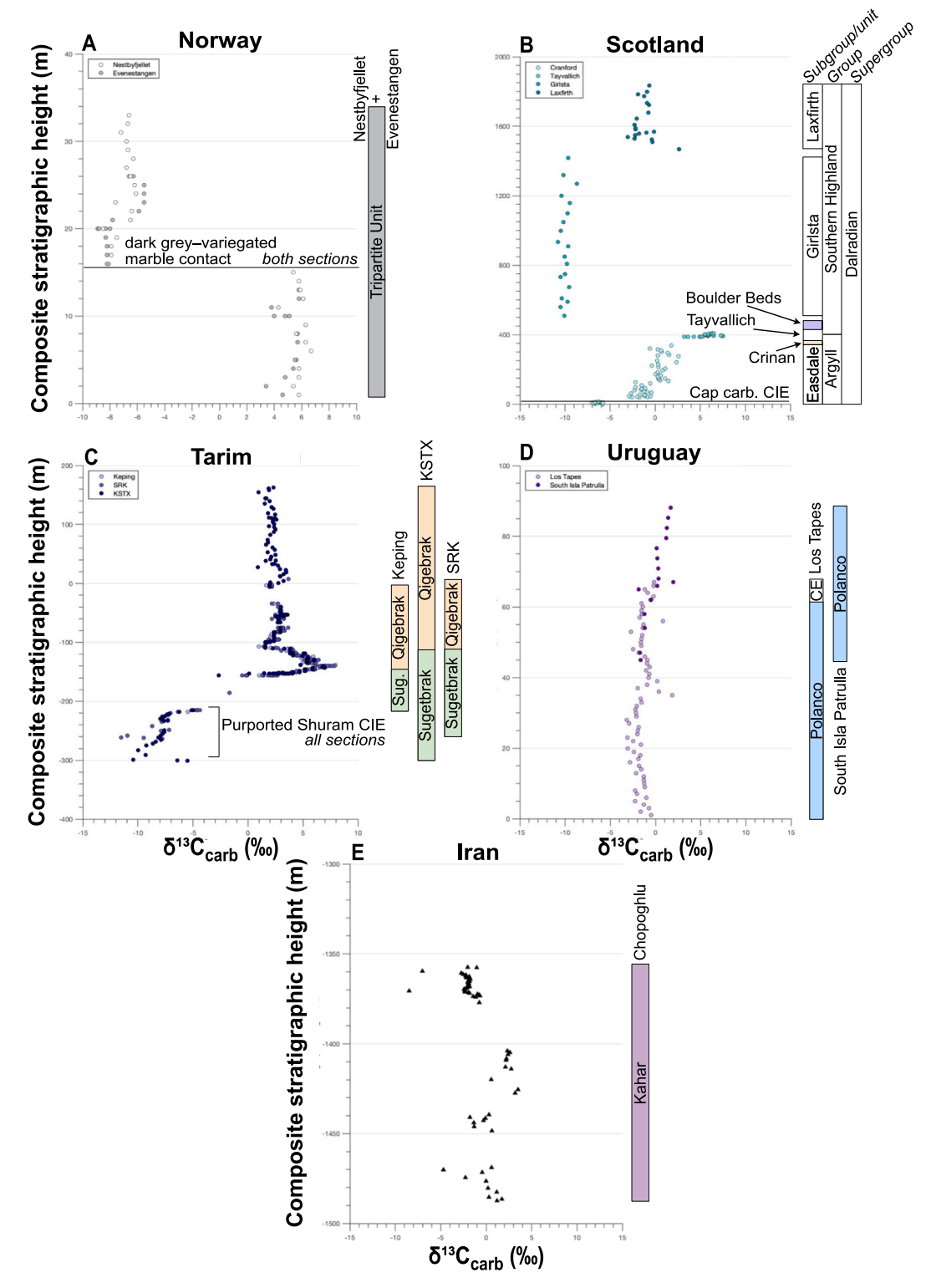


Fig. 4. The DTW $\delta^{13}C_{carb}$ composites for regions with low-resolution $\delta^{13}C_{carb}$ records and no geochronologic constraints (Norway, Scotland, Tarim, Uruguay, and Iran). Each aligned record is color-coded gradationally according to the legend and region (Norway in A; Scotland in B; Tarim in C; Uruguay in D; Iran in E). Refer to Table 1 and text for details on composite construction. Abbreviations as in Fig. 2, Sug. is Sugetbrak Formation, and CE refers to Cerro Espuelitas Formation. Note that Iran is represented by only a single $\delta^{13}C_{carb}$ record and is thus not a composite.

Pearson r in each target—candidate library (herein the $r_{\rm max}$ alignment) closely replicated the published visual correlation (Table 1, column E). However, when the $r_{\rm max}$ alignment notably differed from a published visual correlation, we instead selected a high Pearson r alignment that better conformed to the published correlation. In Table 1 (column E) we designated these as lithology-guided ('lith-guided') alignments and

reported the associated Pearson r in parentheses. While algorithmic alignment can never produce a facsimile of the field expert's correlation, the former method allowed us to merge all the $\delta^{13}C_{\rm carb}$ data points for one region onto a shared temporal axis, an exercise impossible with the eye alone, while still honoring geological observations (e.g., lithostratigraphic parsimony). For chemostratigraphic records without an

Table 1

Regional $\delta^{13}C_{carb}$ composite construction details. Organized information regarding how each composite was constructed, including: A—the short-hand name of the paleo-depositional region, B—the name of the constituent sub-composites, if any, comprising the reginal composite with reference to the chemostratigraphic data, C—the name of the constituent stratigraphic sections and which section was selected as the target record (bolded), D—the references (and figures) that guided dynamic time warping alignment selection, with an indication of previous alignment style (L = 'correlation lines' indicating general proposed chemostratigraphic alignment; P = 'correlated points' indicating specific proposed chemostratigraphic alignment), E—whether the *r*-max alignment solution agrees with the previously proposed correlation, and F—which alignment was selected for inclusion in the composite (including the corresponding *r*, *g*, and *edge* values) (Boggiani et al., 2010; Calver, 2000; Kaufman et al., 2007; Nelson et al., 2023; Pokrovskii et al., 2006; Prave, 1999; Saylor et al., 1998; Summa, 1993; Wood et al., 2015; Zhu et al., 2007).

A—Paleo- Depositional Region	B—Composite Name (Citation for Chemostratigraphic Data)	C—Stratigraphic Sections (Target, Candidate)	D—The published figure(s) that guided the selection of a DTW alignment from a target—candidate alignment library (green font) or the alternative justification (black font).	E—Is the r _{max} DTW alignment consistent with the published correlation (see D)?	F—Selected DTW alignment (Pearson <i>r, g, edge</i>)
	Oman Mountains-Huqf (Khufai and Shuram formatio (Osburn et al., 2015)	ons) sub-composite MDE BD1 BD4	Osburn et al. (2015), Figure 2 (P)	yes	r-max (0.70,0.98,0.04) r-max (0.75,1.01,0.15)
		BD5 BD6 KDE KDS			r-max (0.71,0.98,0.15) r-max (0.66,1.01,0.01) r-max (0.43,1.00,0.12) r-max (0.21,0.99,0.15)
		KDW MD5 MD6		e e	r-max (0.88,0.98,0.15) r-max (0.85,0.98,0.01) r-max (0.88,0.99,0.15)
		NA1 PF1 AQ1 WH1		e e	r-max (0.81,0.99,0.15) r-max (0.42,0.98,0.11) r-max (0.49,0.98,0.15) r-max (0.51,1.01,0.15)
	Jebel Akhdar (Hadash Formation) sub-composite	WM1 WS1		no	r-max (0.83,1.00,0.03) lith-guided (0.76,1.00,0.15)
	(Allen et al., 2004)	Hadash-1 Hadash-2 Wadi Haji-1 Wadi Bani Awf	Allen et al. (2004), Figure 10 (L)	yes "	r-max (0.85,0.99,0.15) r-max (0.66,0.99,0.08) r-max (0.75,0.99,0.08)
	OMAN REGIONAL COMPOSITE (Rooney et al., 2020)	Thamoud-6		-	-
	(Fike et al., 2006)	Migrat-1	Selected the highest Pearson r DTW solution that aligns the CIE in the Shuram Formation in both cores. (Compare Fig. 1 of Fike et al. (2006) (Migrat-1) to Figure 1 of Rooney et al. (2020)(Thamoud-6).)	yes	r-max (0.96,0.98,0.12)
	this study	Oman Mountains-Huqf sub-composite	Selected the highest Pearson r DTW solution that aligns the CIE profile from the Shuram Formation from the Oman Mtns-Huqf and Thamoud 6 (compare Figure 2 of Osburn et al, 2015 to Figure 1 of Rooney et al, 2021).	yes	r-max (0.93,0.98,0.11)
	this study	Jebel Akhdar sub-composite	The Hadash cap carbonate sits stratigraphically below the oldest isotopic values of the Thamoud-6 (compare Figure 13 of Allen et al. 2004, to Figure 1 of Rooney et al., 2021). Thus we manually positioned this section below Thamoud-6.	no	n/a
	(Fike and Grotzinger, 2008)	BB4 MNH1	For TM-6, compare Figure 4 of Fike and Grotzinger (2008) to Figure 1 of Rooney et al. (2020). (See Figure S8.) For BB4 and MNH1, we selected high Pearson r DTW alignments that positioned the BACE following Figure 5 of Fike and Grotzinger	n/a	lith-guided (0.94,0.98,0.15)
	CHINA REGIONAL COMPOSITE	TM6	(2008).	yes	lith-guided (0.18,1.01,0.15) r-max (0.95,0.98,0.01)
	Zhu et al. (2013) Zhu et al. (2007)	Xiangdangping Feidatian Dangahe	Zhu et al. (2007), Figure 20 (T)	no	 lith-guided (0.89,0.98,0.11)
	Yang et al. (2021) Goz A sub-composite	Wenggao1 Wenggao2 Xiajiaomeng	Yang et al. (2021), Figure 1 (L) and Supplmentary Materials (P).	yes	lith-guided (0.90,0.99,0.10) r-max (0.88,1.00,0.06) r-max (0.97,0.99,0.14)
	Macdonald et al. (2013) Goz B sub-composite	F849 F850	We manually stacked these non- or minimally overlapping records following Figure 8 (T) of Macdonald et al. (2013)	n/a	n/a
	Macdonald et al. (2013)	F855 W12 W13 W15	As for the Goz A sub-composite.	n/a	n/a
	Fog Camp sub-composite Macdonald et al. (2013)	F1129 F838	As for the Goz A sub-composite.	n/a	n/a
	Tango Tarn sub-composite Macdonald et al. (2013) Coal Creek sub-composite	J901 F838	We manually stacked these non- or minimally overlapping records following Figure 11 (T) of Macdonald et al. (2013).	n/a	n/a
	Macdonald et al. (2013) Ogilvie Mountains sub-composite	F842	An individual record (Figure 11 of Macdonald et al., 2013).	n/a —	n/a
	this study Wernecke Mountains sub-composite	Tango Tarn sub-composite Coal Creek sub-composite	Macdonald et al. (2013), Figure 11 (T)	- yes	 r-max (0.97,0.98,0.15)
	this study	Goz A sub-composite Goz B sub-composite (lower) Goz B sub-composite (upper) Fog Camp sub-composite	Macdonald et al. (2013), Figure 8 (T)	yes	 r-max (0.67,1.01,0.12) r-max (0.87,1.01,0.15) r-max (0.90,0.99,0.15)
	Central Mackenzie Mountains sub-composite Macdonald et al. (2013) CANADA REGIONAL COMPOSITE	J1132	Individual record (Figure 3 of Macdonald et al., 2013).	n/a	n/a
	this study	Wernecke Mountains sub- composite Ogilvie Mountains sub- Central Mackenzie Mountains	Macdonald et al. (2013), Figure 12 (T)	- no	 lith-guided (0.94,0.98,0.15)
	Zaris sub-basin sub-composite	sub-composite			lith-guided (0.75,0.98,0.02)
	Wood et al. (2015)	Zebra River Brak Omkyk Zwartmodder	Wood et al. (2015), Figure 16 (T)	no	— lith-guided (0.66, 1.01, 0.15) lith-guided (0.75, 0.99, 0.07) lith-guided (0.85, 0.98, 0.15)
	Saylor et al. (1998) Witputs sub-basin sub-composite	Zebra River (S)		yes	r-max (0.89,0.98,0.15)
	Wood et al. (2015)	Grens Arasab		- no	- lith-guided (0.67,1.01,0.15)
	Saylor et al. (1998) Wood et al. (2015) Gariep Belt sub-composite	Swartkloofberg Swartpunt	room or an (Ecolog) i ignie io (1)	yes -	r-max (0.52,0.98,0.15)
	Macdonald et al. (2010)	Namaskluft Farm Dreigratberg Namaskluft Camp	Macdonald et al. (2010), Figure 4 (T)	no yes	lith-guided (0.73,0.99,0.15)
	South Namibia regional composite (Step 1) this study	Zaris sub-basin sub-composi Witputs sub-basin sub- composite	Nelson et al. (2022), Figure 9 (T)		- r-max (0.93,0.98,0.15)
	Nelson et al. (2022) SOUTH NAMIBIA REGIONAL COMPOSITE	(Kuibis Subgroup only) Neint Nababeep (Kuibis Subgroup only)		yes	r-max (0.77,0.98,0.15)
	this study	Witputs sub-basin sub- composite (Schwarzrand Subgroup only)	Nelson et al. (2022), Figure 9 (T)	-	-
		Neint Nababeep (Schwarzrand Subgroup)		yes	r-max (0.65,0.99,0.15)
	Nelson et al. (2022)	Gariep Belt sub-composite	The Dreigratherg and upper Holgat Fms sit stratigraphically below the oldest isotopic values of the Witsput sub-basin (compare Figures 4 of Macdonald et al., 2010, to Figure 9 of Nelson et al., 2022) and, therefore, manually positioned the Gariep Belt sub-composite below the Witsput sub-basin sub-composite.	n/a	n/a

	West Laginha sub-composite				
	Boggiani et al. (2010)	West Laginha West Laginha 'lower'	We manually aligned the higher-resolution section through lower Tamengo Formation with the lower-reso section through the upper Tamengo Fm following Figure 3 (T) of Boggiani et al. (2010).	n/a	n/a
	BRAZIL REGIONAL COMPOSITE this study	West Laginha sub-composite	Participated (ONE) France and (A)	_	-
	Boggiani et al. (2010) Adelaide Rift Complex sub-composite	East Laginha	Boggiani et al. (2010), Figures 3 and 4 (L)	yes	r-max (0.72,0.98,0.15)
	Husson et al. (2015)	MS5 MS1 MS2 MS3 MS4 MS6 MS7 MS8 MS9 MS10 MS10	Husson et al. (2015), Figures 4 and 5 (L)	yes	r-max (0.97,0.98,0.15) r-max (0.99,0.98,0.15) r-max (0.98,0.99,0.15) r-max (0.98,0.99,0.15) r-max (0.98,0.99,0.15) r-max (0.99,0.98,0.15) r-max (0.99,0.98,0.15) r-max (0.99,0.98,0.15) r-max (0.99,0.90,0.15) r-max (0.99,0.00,15) r-max (0.99,0.00,15) r-max (0.99,0.00,15)
	Calver (2000)	MS12 First Hill	For Bunyeroo Gorge, compare Figure 3 (L) and Table 1 of Calver et al. (2000) to the Wonoka and pre-Wonoka formations of Husson et al. (2015). For First Hill, Table 1 of	yes	r-max (0.96,0.98,0.15)
	Olympic Formation (Amadeus Basin) sub-composite	Bunyeroo Gorge	Calver et al. (2000) served as the guide.		r-max (0.98,0.99,0.15)
	Verdel and Campbell (2017) Julie Formation (Amadeus Basin) sub-composite	Olympic 23 Olympic 22 Olympic 28	Verdel and Campbell (2017), Figure 5 (L)	yes	 r-max (0.90,0.98,0.01) r-max (0.40,0.98,0.05)
AUSTRALIA	Verdel and Campbell (2017)	Julie 26 Julie 2 Julie 2 Julie 5 Julie 6 Julie 6 Julie 8 Julie 14 Julie 15 Julie 17 Julie 27	Verdel and Campbell (2017), Figure 6 (L)	yes	r-max (0.85,0.98,0.01) r-max (0.79,0.98,0.15) r-max (0.79,0.98,0.15) r-max (0.79,0.98,0.15) r-max (0.79,0.98,0.15) r-max (0.79,0.08,0.15) r-max (0.75,0.00,0.15) r-max (0.75,1.00,0.15) r-max (0.79,1.00,0.15) r-max (0.69,1.01,0.15)
	Australia regional composite (upper) this study	Adelaide Rift Complex sub- composite	Selected a high Pearson r DTW solution that aligns the CIE profile of the upper Pertatataka and Julie formations to the Wonoka Formation (Shuram CIE) in the Adelaide Rift	-	-
	Australia regional composite (lower)	Julie Formation sub-composite	Complex following Figure 9 of Verdel and Campbell (2017)	no	lith-guided (0.46,1.01,0.01)
	Rose and Maloof (2010), pers. comms. for diachronous composite of Fig. 10c. this study	Nuccaleena Formation sub- composite Olympic Formation sub-compos	Selected the highest Pearson <i>r</i> DTW solution that aligns the cap carbonate CIE of the Olympic and Nuccaleena fms telfollowing Figure 9 of Verdel and Campbell (2017).	- yes	 r-max (0.55,1.00,0.13)
	AUSTRALIA REGIONAL COMPOSITE		The lower (cap carbonate) and upper (Wonoka-equivalent) weAustralia regional composites do not overlap. We manually	-1-	at.
	this study	Australia regional composite (up	stacked these following Figure 9c of Verdel and Campbell	n/a	n/a
	Noonday Formation sub-composite Petterson et al. (2011)	Martin Cabin	,	_	_
	Prave (1999) Petterson et al. (2011)	Southern Nopah Range (ND1) Eastern Wildrose Canyon	Petterson et al. (2011), Figures 5 (T) and 11 (P)	yes	r-max (0.49,1.01,0.03) r-max (0.83,0.98,0.15)
	Lower Johnnie Formation sub-composite	Western Wildrose Canyon			r-max (0.71,0.98,0.15)
	this study Rainstorm Member sub-composite	SN02 SN03 KR01	See unpubulished PhD thesis of Summa (1993).	n/a	 r-max (0.50,0.98,0.07) r-max (0.77,0.98,0.07)
		SN NM	_		r-max (0.99,0.99,0.15)
	Bergmann et al. (2011)	OD SSa	Bergmann et al. (2011), Figure 7 (P)	yes	r-max (0.74,0.98,0.02) r-max (0.58,0.98,0.15)
	Kaufman et al. (2007) Great Basin regional composite (step 1)	Winters Pass Hills			r-max (0.81,0.98,0.15)
(Death Valley, Nevada, and Caborca	Loyd et al. (2012)	Cerro Rajon Cerro El Arpa	Level et al. (2012). Eleven 2 (T)	-	r-max (0.55,0.98,0.01)
	Hodgin et al. (2021)	Cerro San Agustin Death Valley Succession	—Loyd et al. (2012), Figure 2 (T) —and Hodgin et al. (2021), Figure 1 (T)	yes	r-max (0.97,0.99,0.15)
	Loyd et al. (2012) GREAT BASIN REGIONAL COMPOSITE	section)			r-max (0.83,0.98,0.15)*
	this study	Great Basin regional composite (step 1)	Nelson et al. (2023), Figures 1 (L) and 4 (P)	-	=
	Smith et al. (2016)	Mount Dunfee Johnnie-Noonday sub- composite stack (a manual stact of lower Johnnie and Noonday Formation data according to	Selected the highest Pearson r DTW solution that aligns the CIE in the Rainstorm Mbr (Death Valley) and the Clemente Fm (Mexico) and the cap carbonate CIE of the Noonday Fm (Death Valley) and the EI Arpa Fm (Mexico) (following Figure	no	lith-guided (0.97,0.98,0.15)* r-max (0.82,0.99,0.14)*
	this study	respective meterages) Rainstorm sub-composite	2 of Loyd et al., 2012). Selected the highest Pearson r DTW solution that aligns the CIE profile from Rainstorm Member, Johnnie Fm (DV) to the Clemente Formation (Mexico) following Figure 2 of Loyd et al. (2012).	yes	r-max (0.94,1.00,0.15)*
	Krol-Tal sub-composite	Nigalidhar	_	-	
INDIA	Kaufman et al. (2006)	K97.4 K98.1 K97.23 N1–N3 NR S3 K97.5	Kaufman et al. (2006), Figures 5 and 6 (T)	yes	r-max (0.93,1.00,0.08) r-max (0.78,0.98,0.15) r-max (0.75,1.00,0.15) r-max (0.82,0.98,0.15) r-max (0.78,0.99,0.17) r-max (0.78,0.99,0.11) ltth-guided (0.75,0.98,0.15)
	Marwar sub-composite	K97.5 K97.7		no	lith-guided (0.75,0.98,0.15)
	Ansari et al. (2018)	Barna 1 Barna 2	Ansari et al. (2018), Figure 5 (T)	- no	_ lith-guided (0.79,1.00,0.15)
	INDIA REGIONAL COMPOSITE	Krol-Tal sub-composite	Append at al. (2019). Figure 2.71	-	-
	this study Ol and Shuurgat Formations sub-composite	Marwar sub-composite	Ansari et al. (2018), Figure 6 (L)	no	lith-guided (0.57,1.01,0.02)
	Bold et al. (2016) Zuun-Arts Formation sub-composite	Khongor Khevtee Tsakhir Khunkher	Bold et al. (2016), Figure 12 (T)	yes	 r-max (0.91,0.99,0.09) r-max (0.90,0.99,0.15)
MONGOLIA		Bayan SE Bayan	_	-	r-max (0.94,0.98,0.02)
	Smith et al. (2016) MONGOLIA REGIONAL COMPOSITE	SE Bayan Khukh Davaa Tsagaan	Smith et al. (2016), Figure 8 (T)	yes	r-max (0.94,0.98,0.02) r-max (0.90,0.98,0.15) r-max (0.96,0.98,0.12)
	this study NORTH NAMIBIA REGIONAL COMPOSITE	OI + Shuurgat Fm. sub- composite Zuun-Arts Fm. sub-composite	The Zuun-Arts Fm unconformably overlies the Shuurgat Fm such that the sub-composites do not overlap. We manually stacked these following Figure 12 of Bold et al. (2016).	n/a	n/a
	NORTH NAMIBIA REGIONAL COMPOSITE Halverson et al. (2005)	Fransfontein Khowarib Schlucht Okatjovandu	Halverson et al. (2005), Figure 10 (T/P)	- yes	 r-max (0.96, 1.00, 0.15) r-max (0.94, 0.98, 0.09)
		Otjivero Benthansis 5508		no	lith-guided (0.60,1.00,0.02) lith-guided (0.92,0.99,0.15)
	Hoffman and Lamonthe (2019)	Benthansis 5509 Heuwels Macaria Ongongo 1329	Hoffman and Lamothe (2019), Figure 3 (P)	yes no	lith-guided (0.41,1.01,0.08) r-max (0.96,0.99,0.15) lith-guided (0.93,0.98,0.15) lith-guided (0.62,1.00,0.15)
	Culet at (2016)	Ongongo 9001 Tsumeb 1438 Tsumeb 15021	-	yes	r-max (0.91,1.00,0.07) r-max (0.59,1.01,0.02) r-max (0.84,0.99,0.06)
	Cui et al. (2016)	S86A	Cui et al. (2018), Figure 4 (T)		r-max (0.79,0.98,0.07)*

	NORWAY REGIONAL COMPOSITE						
NORWAY	Melezhik et al. (2008)	Nestbyfjellet Evenestangen	Melezhik et al. (2008), Figure 2 (T)	- yes	r-max (0.99,0.98,0.15)		
	SCOTLAND REGIONAL COMPOSITE						
SCOTLAND	Prave et al. (2009)	Cranford Tayvallich Girlsta Laxfirth	The Cranford, Tayvallich, Girlsta, and Laxfirth sections do not overlap and, as such, were manually stacked following Figure 2 (P) of Prave et al. (2009).	n/a	n/a		
	SIBERIA REGIONAL COMPOSITE						
SIBERIA	Pokrovskii et al. (2006)	Zhuya Ura Chara	Pokrovskii et al. (2006), Figure 7 (L)	yes no	r-max (0.98,0.98,0.15) lith-guided (0.23,0.98,0.01)		
SIBERIA	Melezhik et al. (2009)	Bolshoy Patom	Melezhik et al. (2009), Figure 4 (T)	yes	r-max (0.03,0.98,0.02)		
	Cui et al. (2016)	Olenek	The Khorbusuonka and lowermost Kessyusa groups in Arctic Siberia do not overlap. We manually stacked these following Figure 3 of Cui et al. (2016)	n/a	n/a		
	TARIM REGIONAL COMPOSITE						
TARIM	Zhang et al. (2020)	Keping		-	-		
1743 XIIVI	Wang et al. (2022)	KSTX SRK	Compare Figure 11 (L/T) of Wang et al. (2022) to Figure 7 (L) of Zhang et al. (2020).	yes	r-max (0.96,0.98,0.12) r-max (0.98,1.00,0.15)		
URUGUAY	URUGUAY REGIONAL COMPOSITE						
	Aubet al. (2012)	Los Tapes South Isla Patrulla	Aubet et al. (2012), Figures 6 and 7 (L)	– yes	r-max (0.60,0.99,0.15)		
	IRAN (individual section)						
IRAN	Etemad–Saeed et al. (2021)	Chopoghlu section	We adopted the indievidual section reported in Figure 2 of Etemad–Saeed et al. (2021). No alignment required.	n/a	n/a		

illustrated correlation, we defaulted to the r_{max} alignment from the relevant target–candidate alignment library.

Table 1 specifies our method to build each paleo-depositional region's $\delta^{13}C_{carb}$ composite. Headers in Column B (where present) refer to the sub-composites that make up each regional composite; the literature reference for the isotopic data is listed below each header. Column C lists the names of the individual chemostratigraphic sections incorporated into each sub-composite and regional composite; the selected target section is in bold font. Column D indicates, for every target-candidate record pair, which publication and associated figure(s) guided which one of the 60 alignments that we selected to include in the regional composite; if no such previously published alignment exited, text in this column specifies the alternative justification for choosing an alignment. Column E indicates whether the DTW alignment with the maximum Pearson r (' r_{max} ') within each target-candidate alignment library conformed with the visual correlation, if any, in column D. (Note that this does not mean the DTW-guided and visual-guided alignments are identical.) Column F specifies the selected alignment (with the identifying g and edge values, and the associated Pearson's r). Where relevant, the final rows of each regional composite explain how we repeated the above method to align sub-composites to one another when constructing the regional $\delta^{13}C_{carb}$ composite.

Below we walk through one example of how to use Table 1 to reproduce this algorithmic-informed approach to correlation. To build the Oman $\delta^{13}C_{carb}$ regional composite (Table 1, column A) we first constructed two sub-composites (Table 1, column B), one for the Oman Mountains and Huqf (Osburn et al., 2015) and one for Jebel Akhdar (Allen et al., 2004). We selected sections MDE and Hadash-1 as the targets for each respective sub-composite (Table 1, column C, bold names). Fig. 2 of Osburn et al. (2015) presents a chemostratigraphic correlation of the Oman Mountains-Hugf sections as a stack of each δ¹³C_{carb} record atop another; hence, Table 1, column D, indicates that Fig. 2 of Osburn et al. (2015) provides a point-to-point (or type 'P') guide to DTW alignment selection (i.e., which one of the 60 alignments between BD1-MDE was chosen, which one of the 60 alignments between BD4-MDE was chosen, and so forth). We found that the highest Pearson r (r_{max}) alignment in every candidate-target alignment library save for WS-1 was consistent with Fig. 2 of Osburn et al. (2015) (Table 1, column E, fourteen 'yes' and one 'no'). Hence, we selected these 14 r_{max} alignments for the Oman Mountains-Huqf sub-composite (Table 1, column F). For section WS-1, we found an alternative alignment in the library, one with Pearson r of 0.76, and g and edge values of 1.00 and 0.15, respectively, that better conformed to the visual alignment in Fig. 2 of Osburn et al. (2015) and indicated our choice of this lithology-guided (lith-guided) alignment in Table 1, column F. In contrast, for the Jebel Akhdar sub-composite, chemostratigraphic correlation was implied by the broad reproducibility across stratigraphic sections through the Hadash Formation, yet Allen et al. (2004) did not illustrate specific tielines between peaks, nadirs, or inflections (as is common to Ediacaran

chemostratigraphic literature). Hence, we characterized previous correlation of Jebel Akhdar as lithology-informed (type "L") and found that the $r_{\rm max}$ alignment from each candidate—target alignment library conformed with this field expertise.

Finally, to build the overarching Oman regional composite, we selected the Thamoud-6 drill core $\delta^{13}C_{\rm carb}$ record as the target, which shares a lithostratigraphic framework with all additional records for the Oman regional composite. We selected the highest Pearson r DTW solution that aligned the CIE in the Shuram Formation at each candidate record (Miqrat-1, Oman--Mountains Huq sub-composite, and TM-6) to the Shuram Formation CIE in Thamoud-6 (Table 1, column D; Fike et al., 2006; Fike and Grotzinger, 2008; Osburn et al., 2015; Rooney et al., 2020), which in every case was the $r_{\rm max}$ alignment. As the Hadash cap carbonate sits stratigraphically below the oldest isotopic values of Thamoud-6, we manually positioned the Jebel Akhdar sub-composite below Thamoud-6 (Table 1, column D). Finally, for the BB4 and MNH1 records we selected high Pearson r DTW alignments that positioned the isotopic snippets of the BACE in the Ara Formation following Fig. 5 of Fike and Grotzinger (2008).

Figs. 2–4 illustrate the 16 Ediacaran $\delta^{13}C_{carb}$ paleo-depositional regional composites that arise from following the geology-informed alignment selection procedure detailed in Table 1. Each composite shows the constituent sections and/or sub-composites color-coded according to the inset legend. Each composite is annotated with the position of the Marinoan cap-carbonate–hosted carbon isotope excursion (CIE), the Shuram/Wonaka CIE, and the basal Cambrian excursion (BACE), as identified (or hypothesized) by the primary field workers. To the right of each regional composite, we show the aligned position of local lithostratigraphic units to facilitate the evaluation of algorithmic alignments.

2.3. Constructing a Bayesian Markov chain Monte Carlo age model for the Ediacaran Period

2.3.1. Bayesian age-depth modeling and geochronological inputs

Bayesian age–stratigraphic height models generate a median age, and associated 95% confidence interval, by treating sediment accumulation as discrete events drawn from a compound Poisson-gamma probability distribution estimated through Markov Chain Monte Carlo methods (Haslett and Parnell, 2008; Landing et al., 2021; Schoene et al., 2019; Trayler et al., 2019). We constructed a B-McMC age model with open-source code from Schoene et al. (2019) and the following inputs: 10,000 replicates, 10,000 age model paths, and 10,000 stratigraphic beds. We conditioned the B-MCMC age model on 25 U-Pb and Re—Os radioisotopic ages directly tied to $\delta^{13} C_{\rm carb}$ values in the time-calibrated $\delta^{13} C_{\rm carb}$ composite (Table 2; see Section 2.3.2). We took the conservative approach to limit ages to those sampled from stratigraphic sections included in the regional composites (i.e., those with published guidance on how to align); this avoided the circularity that might arise from

extrapolating ages from adjacent sections. More exhaustive compilations of Ediacaran radioisotopic depositional ages exist (Yang et al., 2021), and can guide future iterations. For U-Pb ages, we conditioned the model on $\pm Z$ -uncertainty (Table 2, bold green entries), which vary from ~0.60-0.97 Myr; uncertainty in Re-Os isochron ages vary from 2.8 to 6 Myr. We assigned each age to the stratigraphic meterage of the time-calibrated composite (Table 2; Fig. 5). Take, for example, the 539.41 ± 0.66 (Z-uncertainty) CA-ID-TIMSs zircon U—Pb age from the Spitskop Member of the Schwarzrand Subgroup, Neint Nababeep Plateau; this volcanic ash was assigned to 1533.87 m height in the South Namibia regional composite and, when the latter was aligned to the Oman regional composite, was warped to -1778.28 m in the timecalibrated regional composite meterage. Hence the age mode is conditioned with 539.41 \pm 0.66 at -1778.28 m. We explored 10,000 sediment accumulation histories (age model paths) within these geochronologic uncertainties (Fig. 5b).

2.3.2. Building the $\delta^{13}C_{carb}$ -Bayesian Markov chain Monte Carlo agemodel backbone

We selected the Oman regional composite as the target record for the δ13C_{carb}-Bayesian Markov chain Monte Carlo age-model backbone (Table 3). DTW alignment of the complete regional composites from China and Brazil to the Oman composite produced high Pearson r solutions that chronologically sequenced every age in both the target and candidate composites (Table 3; Fig. 5a). However, for both south Namibia and northwest Canada, DTW alignment yielded zero solutions (out of 60) that chronologically sequenced all ages. (That is, for all 60 alignments, at least one date was out of chronological order.) For this reason, we moved forward by cleaving the south Namibia regional composite into two (Table 3), a lower piece encompassing $\delta^{13}C_{carb}$ values from the Driegratberg and upper Holgat formations (Gariep Belt; (Macdonald et al., 2010) and the Kuibis Subgroup (of the Zaris and Witsput sub-basins and Neint Nababeep Plateau; Nelson et al., 2022) and an upper piece encompassing $\delta^{13}C_{carb}$ values from the upper members of the Schwarzrand Subgroup (Nelson et al., 2022; Table 3; Fig. S16). After normalizing the former, we identified an alignment (r =0.82) that abided by the available geochronologic constraints and the published stratigraphic correlations (Fig. 5a). For the latter piece, the 539.63 ± 0.15 Ma age in the Huns Member and the enriched isotopic values together suggest that the Schwarzrand Subgroup stratigraphy is not time-equivalent to the Ara Group, Oman, whose youngest age, 541.0 \pm 0.8, occurs in more depleted $\delta^{13}C_{carb}$ values (Nelson et al., 2022). Therefore, we manually stacked this piece above the Oman regional composite.

We cleaved the northwest Canada regional composite into four pieces before aligning them to the Oman regional composite: one encompassing the CIE profile of the Ravensthroat and Sheepbed formations, a second capturing the positive $\delta^{13}C_{carb}$ values immediately prior to the Shuram excursion (the Sheepbed carbonate), a third capturing the Shuram CIE in the June Beds and Game Trail Formation, and a fourth capturing the Blue Flower and Risky Formations (lithostratigraphy sensu Macdonald et al., 2013). The r_{max} alignment between the latter two cleaved pieces and the Oman regional composite conformed with previously proposed stratigraphic correlations (Table 3). We found an alignment between the $\delta^{13}C_{\text{carb}}$ profile of the June Beds and Game Trail formations (northwest Canada) and the Khufai and Shuram formations (Oman) only after normalizing the $\delta^{13}C_{carb}$ records (normalized r_{max} alignment, r = 0.98). Lastly, we selected a high Pearson *r* alignment (r = 0.86) that aligned the $\delta^{13}C_{carb}$ profile in the Blue Flower and Risky formatons to the Buah Formation and Ara Group of Oman (Fig. 5a).

Because DTW alignments include many–to–one point assignments between a candidate and target section (Section 2.1; Fig. 1c) there were three instances in which two radiometric dates were assigned to the same height in the time-calibrated $\delta^{13}C_{carb}$ composite: the 557.0 \pm 3.0 Ma and 556.38 \pm 0.7 Ma ages (China) were assigned to the time-

calibrated composite at -2395 m; the 547.36 ± 0.91 Ma and 545.27 \pm 0.61 Ma ages (south Namibia) were assigned to -2255 m, and the two ages from Brazil, 542.37 \pm 0.68 and 541.85 \pm 0.97, were assigned to -2158 m (Fig. 5). This outcome does *not* mean these dated strata are the same age; the ages are distinct from one other both analytically and stratigraphically. Instead, the DTW alignment predicts that, at these horizons, Oman stratigraphic accumulation is condensed relative to the candidate composites. Fig. 1c illustrates an analogous case where four isotopic values with two stratigrahically distinct dates, 557.0 \pm 3.0 Ma and 556.38 \pm 0.7 Ma (blue chemostratigraphic record) are aligned to a single isotopic value (green chemostratigraphic record). Hence, DTW predicts that four chemostratigraphic values accumulated at one location (blue) over a time in which only one isotopic value accumulated at another location (green). For all three cases, we assigned the 'condensed' horizon the mean age and uncertainty of the two radiometric ages.

Fig. 5b shows the median age estimates and 95% confidence interval (97.5th percentile age minus 2.5th percentile) for the chemostratigraphic horizons in the Oman, northwest Canada, China, Brazil, and south Namibia regional composites.

2.4. Constructing the global Ediacaran $\delta^{13}C_{carb}$ composite—Bayesian age model

We constructed the global Ediacaran $\delta^{13}C_{carb}\!-\!B\!-\!McMC$ age model (Fig. 6a) by aligning the eleven temporally unconstrained paleodepositional region $\delta^{13}C_{carb}$ composites (Figs. 3, 4) to the timecalibrated composite (Fig. 5). Table 3 (column C) states the publication and figure of the geological expertise that guided our selection of the DTW alignments to the time-calibrated composite, discussed in further detail below. In this $\delta^{13}C_{carb}$ -Bayesian age model, each $\delta^{13}C_{carb}$ value from a temporally unconstrained composite takes on the median age and uncertainty of the horizon to which that value aligns (see Fig. 1C where the $\delta^{13}C_{carb}$ value of the green curve is assigned the age of 562.7 \pm 3.8 Ma). However, when multiple time-calibrated $\delta^{13} C_{carb}$ values are aligned to a single undated $\delta^{13}C_{carb}$ value, the age of the oldest value is extrapolated to the previously undated $\delta^{13}C_{carb}$ value. When multiple undated $\delta^{13}C_{carb}$ values are assigned to one time-calibrated composite horizon ($\delta^{13}C_{carb}$ value), the former are assumed to be synchronous within uncertainty of the age of the dated horizon.

As was the case when constructing the regional composites, many alignment libraries contained multiple alignments that are permissible within the uncertainty of geological observations. While some alignments display on minor differences, such as the shift of only one or two isotopic values relative to the alignment selected, other alignments display more substantial stretching and squeezing of candidate $\delta^{13}C_{\text{carb}}$ values relative to the target record. Each permissible alignment makes a different prediction for the time-history of sedimentation in each region. We have chosen just one time history, which may not be accurate—and therefore have generated a working hypothesis, not an unassailable chronology.

2.4.1. Australia

We split the Australia regional composite into two pieces prior to alignment in accord with the gap between the Nuccaleena and Olympic formations (Rose and Maloof, 2010; Verdel and Campbell, 2017) and the Wonoka and Julie formations (Husson et al., 2015; Verdel and Campbell, 2017). We adopted the r_{max} alignment for the former, which situates the cap carbonate CIE against the Hadash–Ravensthroat–Doushantuo Unit I–Dreigratberg. A high Pearson r alignment (r=0.88) situated the Wonoka Formation to other Shuram CIE–equivalent strata in a manner more consistent than the r_{max} alignment (Fig. 6; Table 3).

2.4.2. Great Basin

The alignment library included two *lith-guided* alignments that were similar in their alignment of the CIE of Noonday Formation to the CIE in

the Hadash Formation, and the CIEs in the Rainstorm Member (Johnnie Formation) and Clemente Formation to the CIE in the Shuram Formation (Bergmann et al., 2011; Corsetti and Kaufman, 2003; Creveling et al., 2016; Hodgin et al., 2021; Loyd et al., 2012; Petterson et al., 2011; Smith et al., 2016b). The $\it lith-guided$ alignments differed in the predicted alignment of the BACE, with one predicting the CIE nadir at 540.8 \pm 0.6 Ma and the other at <537.95 \pm 0.54 Ma (above our stratigraphically highest age constraint). We utilized the maximum depositional age of \leq 539.40 \pm 0.23 Ma from Cerro Rajón (Hodgin et al., 2021) to exclude the former alignment and, therefore, selected the latter for the global Ediacaran $\delta^{13}C_{carb}$ –Bayesian McMC age model (Fig. 6).

2.4.3. India

Multiple alignments approximate the proposed stratigraphic correlations for the Ediacaran India stratigraphy (Ansari et al., 2018; Kaufman et al., 2006). We selected a high Pearson r alignment (r=0.87) that aligns the cap-carbonate Blaini Formation to the cap-carbonate Hadash Formation, as well as the large negative carbon isotope excursion ('N3' in Kaufman et al., 2006) at the Krol B–Krol C boundary with the Shuram excursion (Figs. 6 and S29).

2.4.4. Iran

We identified a *lith-guided* alignment (r=0.54) that positions the Iran $\delta^{13}C_{carb}$ record (Chopoghlu section) against the $\delta^{13}C_{carb}$ profile of the Ara Formation (Oman) in the temporally constrained composite (Fig. 6), consistent the hypothesis of Etemad-Saeed et al. (2021).

2.4.5. Mongolia

Bold et al. (2016) and Smith et al. (2016a, 2016b) reported an ~40 Myr unconformity separating the Ol and Shuurgat formations from the Zuun-Arts Formation. Because of this we separately aligned these subcomposites (Table 1) to the temporally constrained composite (Table 3). For the Ol + Shuurgat fms. sub-composite, multiple alignments place the entirety of the Ediacaran Mongolia stratigraphy in line with the Hadash, Masirah Bay, and Khufai formations of Oman. Of these, we selected a high Pearson r alignment (r = 0.88) that most closely matched the previously proposed stratigraphic correlation, positioning the top of the Shuurgat Formation below the top of the Khufai Formation of Oman (Bold et al., 2016). For the Zuun-Arts Formation sub-composite, we identified a *lith-guided* alignment (r = 0.45) that positions the base of the Zuun-Arts Formation in the lower Ara Formation of Oman with the upper Zuun-Arts Formation extending above the top of the Ara Formation (with a similar stratigraphic positioning as the upper Kuibis and Schwarzrand sub-groups in South Namibia and the Wood Canyon, La Ciénega, and Dunfee formations from the Great Basin).

2.4.6. Northern Namibia

There are no geochronologic constraints from northern Namibia, yet the lithostratigraphy and $\delta^{13}C_{carb}$ profile of the Maieberg, Elandshoek, and Huttenberg formations (Tsumeb Subgroup) and equivalent Karibib Formation are considered equivalent to the Marinoan (basal Ediacaran) cap carbonate and overlying succession (Cui et al., 2018; Halverson et al., 2005; Hoffman and Lamothe, 2019). The r_{max} alignment (r = 0.92)

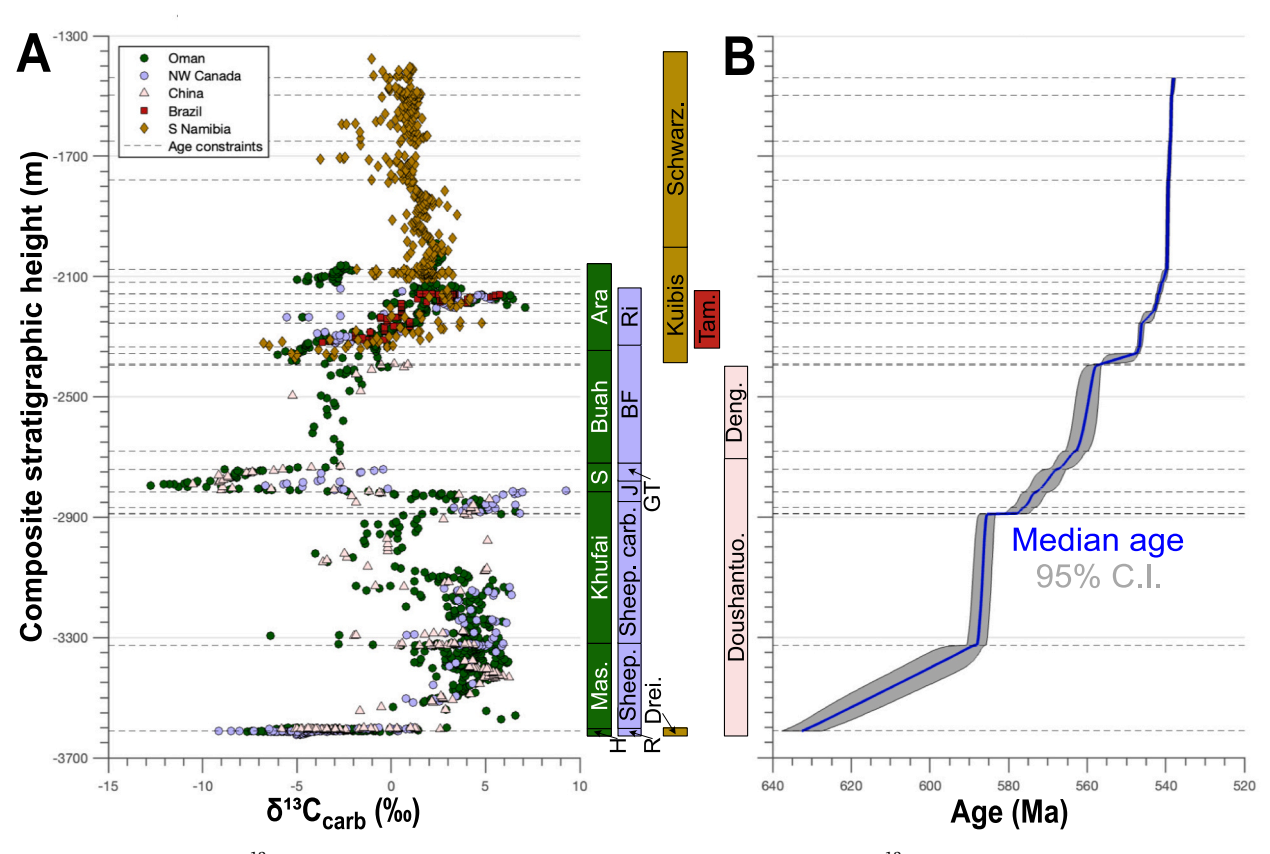


Fig. 5. The time-calibrated $\delta^{13}C_{carb}$ composite and coupled Bayesian age model. A, The age-calibrated $\delta^{13}C_{carb}$ composite, see Table 3 for details on its construction (see key for coloring). The composite stratigraphic height refers to the Oman regional composite meterage (the target record). Dashed black lines indicate the position of all 25 geochronologic age constraints (see Table 2) from these temporally constrained $\delta^{13}C_{carb}$ records. Corresponding lithostratigraphic units are color-coded and indicated on the right. B, the resulting Bayesian Markov chain Monte Carlo age model with the median age shown in blue and the 95% confidence interval shown in grey. (For interpretation of the references to color in this figure legend, the reader is referred to the web version of this article.)

Table 2

Geochronologic age constraints incorporated in the time-calibrated composite $\delta^{13}C_{carb}$ record. Each age, along with its uncertainty, meterage in the regional composite (RC), and meterage in the time-calibrated composite (TC) is supplied. Adapted from Yang et al. (2021). (Basei et al., 2011; Beasecker et al., 2020; Canfield et al., 2020; Chen et al., 2020; Grazhdankin et al., 2011; Huang et al., 2020; Liu et al., 2009; Llanos et al., 2005; Matthews et al., 2020; Noble et al., 2015; Parry et al., 2017; Soldatenko et al., 2019; Yang et al., 2017; Zhou et al., 2018).

Region	Age (Ma ± uncertainty)	Regional composite meterage (m)	Time-calibrated composite meterage (m; Figure #)	Reference(s)
	635.23 ± 1.1			Condon et al. (2005)
	632.5 ± 1			Condon et al. (2005)
	614.0 ± 7.6*			Liu et al. (2009)
	612.48 ± 0.9			Yang et al. (2021)
	587.5 ± 3.6*	49	-3326 (Figure 3)	Yang et al. (2021)
	585.7 ± 2.8*	91	-2890 (Figure 3)	Yang et al. (2021)
	557.0 ± 3.0*	158.3	-2395 (Figure 3)	Zhou et al. (2018)
	556.38 ± 0.65	160.45	-2395 (Figure 3)	Yang et al. (2021)
China	556.26 ± 0.65	168.19	-2390 (Figure 3)	Yang et al. (2021)
	554.29 ± 0.63			Yang et al. (2021)
	554.2 ± 3.3*			Chen et al. (2020)
	550.6 ± 3.3*			Chen et al. (2020)
	550.14 ± 0.6			Yang et al. (2021)
	550.0 ± 3.0*			Zhou et al. (2018)
	546.25 ± 0.6			Yang et al. (2021)
	545.76 ± 0.66			Yang et al. (2017)
	543.4 ± 3.5*			Huang et al. (2019)
	621.04 ± 0.90			Bowring et al. (2007)
	578.2 ± 5.9*	-2867	-2867 (Figure 2)	Rooney et al. (2020)
	562.7 ± 3.8*	-2680	-2680 (Figure 2)	Rooney et al. (2020)
_	547.23 ± 0.96	-2355	-2355 (Figure 2)	Bowring et al. (2007)
Oman	546.72 ± 0.89	-2335	-2335 (Figure 2)	Bowring et al. (2007)
	542.90 ± 0.80	-2215	-2215 (Figure 2)	Bowring et al. (2007)
	542.54 ± 1.13			Bowring et al. (2007)
	542.33 ± 0.79	-2190	-2190 (Figure 2)	Bowring et al. (2007)
	541.0 ± 0.81	-2120	-2120 (Figure 2)	Bowring et al. (2007)
	632.6 ± 6.3	-388.3	-3611.59 (Figure 3)	Rooney et al. (2015)
Canada	575.0 ± 5.1*	104	-2888 (Figure 3)	Rooney et al. (2020)
	574.0 ± 4.7*	143	-2817.36 (Figure 3)	Rooney et al. (2020)
	567.3 ± 3.0*	242	-2740 (Figure 3)	Rooney et al. (2020)
	639.29 ± 0.75			Prave et al. (2016)
	635.21 ± 0.92			Prave et al. (2016)
	547.36 ± 0.91	121.9	-2255 (Figure 3)	Bowring et al. (2007)
	545.27 ± 0.61	145.3	-2255 (Figure 3)	Nelson et al. (2022)
South Namibia	539.63 ± 0.64	1236.56	-2075.58 (Figure 3)	Nelson et al. (2022)
	539.41 ± 0.66	1533.87	-1778.28 (Figure 3)	Nelson et al. (2022)
	538.74 ± 0.63	1663.07	-1649.08 (Figure 3)	Nelson et al. (2022)
	538.57 ± 0.60	1815.77	-1496.38 (Figure 3)	Nelson et al. (2022)
	538.04 ± 0.63	1872.77	-1439.38 (Figure 3)	Nelson et al. (2022)
	537.95 ± 0.68			Nelson et al. (2022)
	563.0 ± 3.3*			Becker-Kerber et al. (2020)
	558.0 ± 6.6*			Basei et al. (2010)
Brazil	555.18 ± 0.70			Parry et al. (2017)
	542.37 ± 0.68	504.5	-2158 (Figure 3)	Parry et al. (2017)
	541.85 ± 0.97	518.1	-2158 (Figure 3)	Parry et al. (2017)
	580.90 ± 0.82			Pu et al. (2016)
	580.34 ± 0.88			Pu et al. (2016)
	579.88 ± 0.81			Pu et al. (2016)
	579.63 ± 0.68			Pu et al. (2016)
	579.35 ± 0.75			Pu et al. (2016)
Nourfourding	579.24 ± 0.69			Pu et al. (2016)
Newfoundland	574.17 ± 0.66			Matthews et al. (2020)
	571.38 ± 0.66			Matthews et al. (2020)
	567.63 ± 0.66			Matthews et al. (2020)
	565.0 ± 0.64			Matthews et al. (2020)
	564.71 ± 0.88			Matthews et al. (2020)
	564.13 ± 0.65			Matthews et al. (2020)
	562.5 ± 1.1*			Canfield et al. (2020)
	613.0* 612.15 ± 1.14			Noble et al. (2015) Noble et al. (2015)
England	611.71 ± 1.05			Noble et al. (2015)
	611.71 ± 1.05			Noble et al. (2015)
	569.08 ± 0.94			Noble et al. (2015) Noble et al. (2015)
	565.22 ± 0.89			Noble et al. (2015)
	561.85 ± 0.89			Noble et al. (2015)
	556.6 ± 6.4*			Noble et al. (2015) Noble et al. (2015)
	567.2 ± 3.9*			Grazhdankin et al. (2011)
	556.78 ± 0.62			Soldatenko et al. (2011)
Fast Furoncan	556.78 ± 0.62 555.4 ± 2.9*			Soldatenko et al. (2019) Soldatenko et al. (2019)
East European Platform	555.4 ± 2.9° 557.28 ± 0.63			Yang et al. (2021)
, agom	557.28 ± 0.63 552.96 ± 0.66			Yang et al. (2021) Yang et al. (2021)
	550.2 ± 4.6*			Llanos et al. (2005)
Siberia	543.9 ± 0.24*			Bowring et al. (1993)
SISCIIG	343.5 ± 0.24			Downing et al. (1993)

compares these formations to the Hadash, Masirah, and Khufai formations of Oman (as well as the Ol and Shuurgat formations of Mongolia), and predicts that deposition of the sections comprising the northern Namibia subcomposite occurred from $>\!\!632.58$ Ma (the base of the northern Namibia regional composite aligns below the lowest B-McMC age constraint) to 575.1 ± 4.1 Ma.

2.4.7. Norway

While no geochronology constrains the Norway regional composite, Melezhik et al. (2008) argued that the $\delta^{13}C_{\rm carb}$ profile is consistent with the Shuram excursion. The r_{max} alignment (r=0.75) predicts an equivalence to the Shuram excursion (Fig. 6).

2.4.8. Scotland

Prave et al. (2009) proposed that the Cranford Limestone is a cap carbonate and that the Girlsta Limestone CIE is equivalent to the Shuram excursion (and older than a \sim 601 Ma ash bed). The r_{max} alignment (r=0.88) agrees with these hypothesized correlations (Fig. 6).

2.4.9. Siberia

Melezhik et al. (2009) proposed that the CIE within the Dzhemkukan Formation (Zhuya section) correlates with basal Ediacaran cap carbonate units and that CIE within the Nikol'skoe– Chencha– Zherba formations is equivalent to the Shuram–Wonoka excursion. The r_{max} solution (r=0.87) is consistent with this correlation. In Arctic Siberia, a diatreme in a nearby section yields a minimum age of 543.9 \pm 0.24 Ma for the Kyatyspyt Formation, Olenek section (Bowring et al., 1993; Cui et al., 2016). The r_{max} alignment predicts that the Olenek section was deposited from 567.4 \pm 2.4 Ma to 546.9 \pm 0.5 Ma with the skeletal fossils first appearances occurring in the second half of this range: *Khatyspytia* at 559.3 \pm 3.4 Ma and both *Charnia* and *Hiemalora* at 558.1 \pm 2.4 Ma.

2.4.10. Tarim

Wang et al. (2022) proposed that the $\delta^{13}C_{carb}$ profile of the Sugetbrak and Qiegbrak formations is correlative to the Shuram, Buah, and Ara formations of Oman (see their Fig. 12). Two geochronologic constraints support this correlation. First, detrital zircons from a sandstone stratigraphically underlying the Sugetbrak Formation yield a maximum depositional age of \leq 588 \pm 12 Ma (Zhu et al., 2011). Second, a syndepositional cement from the upper Qiegbrak Formation has been dated to 542.7 \pm 8.0 Ma (Yang et al., 2020). The r_{max} solution (r = 0.91) between the Tarim regional composite and the temporally calibrated composite conforms with these constraints, and predicts an age of 542.2 \pm 0.4 Ma for the stratum that hosts the syndepositional cement, within the U/Pbage uncertainty (Fig. 6).

2.4.11. Uruguay

The r_{max} alignment (r=0.63) between the Uruguay regional composite (Polanco Formation) and the temporally constrained composite predicts that deposition occurred from 585.1 ± 2.3 Ma to 583.2 ± 2.4 Ma, consistent with the maximum age constraint of $\sim\!600$ Ma (from K—Ar geochronology of diagenetic illite in the underlying Yerbal Formation) and a minimum age of $\sim\!566$ Ma (from the youngest detrital zircon U—Pb age from the overlying Barriga Negra Formation; see summary in Aubet et al., 2012).

3. The global Ediacaran DTW-based $\delta^{13} C_{carb}$ composite–Bayesian age model

The DTW-based global Ediacaran $\delta^{13}C_{carb}$ composite—Bayesian McMC age model spans from 632.5 ± 5.3 Ma to 538.0 ± 0.5 Ma (Fig. 6b). For some intervals, the DTW global $\delta^{13}C_{carb}$ composite shows discernable $\delta^{13}C_{carb}$ trends, which we term coherent structure; examples of coherent structure include the negative CIE associated with the basal Ediacaran cap carbonates and the negative CIE associated with the Shuram excursion (Fig. 6a). For other intervals, however, the DTW global $\delta^{13}C_{carb}$ composite shows high variance in either or both of: the point-to-point differences between isotopic ratios of successive stratigraphic samples and the isotopic ratio from different regions. For example, the $\sim\!20$ Myr following the Marinoan cap carbonate CIE shows higher variance (Fig. 6a).

Around ${\sim}610$ Ma, the $\delta^{13}C_{carb}$ profile shows a greater density of data with greater coherence, displaying a positive or invariant trend until ${\sim}590$ Ma (although $\delta^{13}C_{carb}$ values still display variability of upwards of 5‰ across paleobasins). Around ${\sim}590$ Ma, $\delta^{13}C_{carb}$ values trend negative, capturing a smaller negative CIE that precedes the Shuram excursion (equivalent to the 'N3' excursion in China; Zhu et al., 2013). Above this, the selected dynamic time warping alignments predict that no $\delta^{13}C_{carb}$ values represent the timespan from 585.38 \pm 2.57–577.87 \pm

3.80 Ma. The $\delta^{13}C_{carb}$ record is then predicted to resume with the coherent Shuram excursion; at Oman, this excursion is predicted to begin at 574.62 \pm 3.70 Ma before reaching the nadir at 571.11 \pm 4.25 Ma (Table 4, see Section 4). These alignment selections also predict that $\delta^{13}C_{carb}$ values had recovered to >-5% by $\sim\!566$ Ma at all paleobasins with a purported Shuram excursion (Table 3, see Section 4). Further these alignments predict an interval of high variance in $\delta^{13}C_{carb}$ values from $\sim\!565$ Ma to $\sim\!547$ Ma. Finally, the DTW alignments predict quasiperiodic variation in chemostratigraphic records, with $\delta^{13}C_{carb}$ values fluctuating between $\sim-5\%$ and 5%, with four excursions spanning the time from 547.23 \pm 0.81 to 537.95 \pm 0.53 Ma.

4. Utility of the Ediacaran global composite $\delta^{13}\text{C}_{\text{carb}}\text{-Bayesian}$ age model

Stratigraphic alignment stands as a continual work in progress—and algorithmic alignment is no exception. Future improvements to dynamic time-warping composite construction should innovate probabilistic outcomes that incorporate, for example, analytical uncertainty in $\delta^{13} C_{\text{carb}}$ values to alignment; select not just one, but all geologically permissible alignments from a target–candidate alignment library; and consider permutations arising from alternative target record selection. In turn, probabilistic temporal sequencings will demand further complexity from Bayesian age-depth models when priors—for example, stratigraphic position—are themselves probability distributions. Yet, the present Ediacaran global composite $\delta^{13} C_{\text{carb}}$ –Bayesian age model prediction, while a stepping stone, offers ample fodder for discussion of outstanding Ediacaran geobiological, geochemical, and paleoclimatic questions.

The basal Ediacaran, Shuram and 'BACE' carbon isotopic excursions have each been forwarded as prominent magnitude excursions readily correlatable between distant paleogeographic regions, although dissenting views exist for each case. Yet, we found that dynamic timewarping guided alignment of CIE nadirs was more easily achieved for the Shuram than the BACE (Fig. 7).

The selected DTW alignments position each purported Shuram CIE as equivalent to the Shuram excursion sensu stricto from the Shuram Formation, Oman, yet the resulting alignments position the nadir from each paleobasin at different times (Table 4; Fig. 7a). For the case of the Shuram CIE, the shared temporal framework allows us to calculate simple quantitative metrics for correlative chemostratigraphic events (Fig. 7a). For example, we calculated five metrics for the Shuram CIE (sensu stricto from Oman) and those CIEs aligned to the Shuram (Table 4): t_0 and t_n , the estimated age of the local onset (most positive value immediately preceding the initial negative limb of the excursion) and local nadir of the excursion (the most negative value reached during the excursion), respectively; t_{n-0} , the time from the onset to the nadir of the excursion; t_r , the time to return from the local nadir to a $\delta^{13}C_{carb}$ value of -5% (an arbitrary threshold); and m_n , the magnitude of the excursion from t_0 and t_n . The selected DTW alignments predict an onset age that varies from 574.62 \pm 3.7 Ma (Oman, Great Basin) to 572.48 \pm 3.71 Ma (northwest Canada) and an age of the nadir that ranges from 572.23 \pm 4.03 Ma (Norway) to 570.49 \pm 4.32 Ma (China). Hence the predicted local times to nadir, $t_{\text{n-o}}$, vary from as long as 3.98 \pm 5.67 Myr (China) to as rapid as 0.52 ± 5.59 Myr (Norway), with a mean duration of 2.06 \pm 1.87 Myr. Likewise, the local recovery times, t_r , vary from 0.62 \pm 5.78 (northwest Canada) to 5.11 \pm 5.69 (Siberia), with a mean duration of 3.56 \pm 1.92 Myr. In light of observations that m_n varies by paleo-depositional region, from 12.3 to 17.5% (average \sim 15%), these B-McMC age model duration estimates predict that any proposed causal mechanism for the Shuram CIE should be able to achieve a depletion of \sim 15‰ within a mean time of 2.06 \pm 1.87 Myr (Table 4). These metrics do not require the Shuram excursion to be asynchronous, and can instead arise from stratigraphic incompleteness (e.g., the most negative isotopic ratio captured locally need not be the most negative isotopic ratio achieved). Hence the age model—built on a least-squares

Table 3

Age-calibrated $8^{13}C_{carb}$ composite and global Ediacaran $8^{13}C_{carb}$ composite construction details. Organized information regarding how the five age-calibrated regional composites were aligned with the Oman regional composite as the target record. B—the regional composite name, C—the geological and chemostratigraphic observations that guided the selection of the DTW alignment, D—whether the *r-max* alignment solution agrees with the previously proposed correlation, and E—which alignment was selected for inclusion in the composite (including the corresponding r, g, and edge values) (Zhang et al., 2020).

—DTW Composite Name	B—Regional Composite Name (see Table 1) Target. Candidate.	C—The geological observations that guided the selection of the DTW alignment (see column E).	D—Is the r_{max} DTW alignment consistent with the geological rationale (column C)?	E—Selected DTW alignment (Pearson <i>r, g, edge</i>)
	Oman regional composite		-	-
	China regional composite	Selected a high Pearson r DTW solution that (i) chronologically sequenced radioisotopic ages (Table 2) and aligned (ii) the CIE in Duoshantuo Fm (unit I) to the Hadash Fm, Oman and (iii) the CIE in Duoshantuo (unit III) to the Shuram Fm, Oman (consistent with Rooney et al., 2020, Figure 1; Yang et al., 2021, Figure 2). The geochronological sequencing aligns the Dengying Fm below the Ara Group, Oman, consistent with Yang et al. (2021), though different from Rooney et al. (2020).	no	geochron-guided (0.91,1.00,0.11)
	Brazil regional composite	Selected a high Pearson r DTW solution that chronologically sequenced radioisotopic ages (Table 2).	no	geochron-guided (0.50,0.99,0.15)
	South Namibia regional composite (Gariep Belt sub-composite and Kuibis Subgroup)	Selected a high Pearson r DTW solution that (i) chronologically sequenced radioisotopic ages (Table 2) and (ii) aligned the Gariep Belt subcomposite cap carbonate CIE to the Hadash Formation, Oman (consistent with Rooney et al., 2020, Figure 1; Yang et al., 2021, Figure 2);	no	geochron-guided (0.82,0.98,0.15)*
	South Namibia regional composite (Schwarzrand Subgroup)	The 539.63 +/- 0.15 Ma age in the Huns Mbr., as well as the enriched isotopic values, suggests that Schwarzrand Subgroup stratigraphy is not time-equivalent to the Ara Group, Oman, whose youngest age, 541.0 +/- 0.8, occurs in more depleted d13Ccarb values. Therefore, we manually stacked this composite above the Oman regional composite.	n/a	n/a
	Canada regional composite (Ravensthroat–Sheepbed fms.)	Selected a high Pearson r DTW solution that (i) chronologically sequenced radioisotopic ages (Table 2) and (ii) aligned the Ravensthroat cap carbonate CIE to the Hadash Formation, Oman (consistent with Macdonald et al., 2013, Figure 13 and Rooney et al., 2020, Figure 1).	yes	r-max (0.92,0.99,0.16)
	Canada regional composite (Sheepbed carbonate)	Selected a high Pearson r DTW solution that (i) chronologically sequenced radioisotopic ages (Table 2) and (ii) aligned the Sheepbed carbonate CIE to the Khufai Fin, Oman. This is consistent with Rooney et al., 2020; Figure 1 and Yang et al., 2021; but officers from Figure 13 of Madoonald et al. (2013) which aligned the Sheepbed carbonate with the Massirah Bay Fin, Oman.	yes	r-max (0.81,1.00,0.15)
	Canada regional composite (June Beds-Game Trail fms.)	Selected a high Pearson r DTW solution that (i) chronologically sequenced radioisotopic ages (Table 2) and (ii) aligned the June Beds and Gametrall CIE to the Khufai and Shuram Fins, Oman, consistent with Madonald et al., 2010, Figure 13; Rooney et al., 2020, Figure 1; and Yang et al., 2021, Figure 1.	yes	r-max (0.98,0.98,0.15)*
	Selected a high Pearson r DTW solution that (i) chronologically sequenced radioisotopic ages (Table 2) and (ii) aligned the Blue Flower and Risky Fms CIE profile to the Buah Fm and Ara Group. Oman. consistent with Madonald et al., 2010, Figure 13; Rooney et al., 2020, Figure 1; and Yang et al., 2021.		no	geochron-guided (0.86,1.00,0.14)
	Age calibrated composite		=	=
	Australia regional composite (cap carbonate units)	— Guided by Figure 9 of Verdel and Campbell (2019). See section 2.4.1	yes	r-max (0.44,0.99,0.03)
	Australia regional composite (post cap-carbonate units)	Outdoo by Figure 3 of Verder and Oampoon (2013), See Section 2.4.1		lith-guided (0.88,0.99,0.15)
	Great Basin regional composite	Guided by Figure 11 of Peterson et al. (2011), Figure 2 of Loyd et al. (2012), and Figure 1 of Hodgin et al. (2021). See section 2.4.2	no	lith-guided (0.85,1.00,0.15)
	India regional composite	Guided by Figure 5 of Ansari et al. (2018). See section 2.4.3		lith-guided (0.87,1.00,0.15)
LOBAL EDIACARAN COMPOSITE	Iran (Chopoghlu section)	Guided by Figure 8 of Etemad–Saeed et al. (2021). See section 2.4.4		lith-guided (0.54,1.00,0.15)
	Mongolia regional composite (OI+Shuurgat fms.)	Guided by Figure 17 of Bold et al. (2016). See section 2.4.5		lith-guided (0.88,1.00,0.07)
	Mongolia regional composite (Zuun-Arts Fm.)	Guided by Figure 12 of Smith et al. (2016). See section 2.4.5		lith-guided (0.45,1.01,0.01)
	Northern Namibia regional composite	Guided by Figure 4 of Cui et al. (2018) and Figures 1 and 3 of Hoffman and Lamothe et al. (2019). See section 2.4.6	_	r-max (0.92,0.98,0.15)
	Norway regional composite	Guided by Figure 4 of Melezhik et al. (2008). See section 2.4.7	_	r-max (0.75,1.00,0.15)
	Scotland regional composite	Guided by Figure 2 of Prave et al. (2009). See section 2.4.8	yes	r-max (0.88,0.98,0.15)
	Siberia regional composite	Guided by Figures 1 and 4 of Meleżnik et al. (2009) and Figures 3 and 7 of Curlet al.		r-max (0.87,0.98,0.15)
	Tarim regional composite	G0160 S97 (G01657 2010 or znang et al. (2020) and inigure 12 or wang et al. (2022).		r-max (0.91,0.99,0.15)
		Guided by discussion in Aubet et al. (2012). See section 2.4.11		r-max (0.63,1.01,0.04)

algorithm designed to align or synchronize values—cannot objectively assess synchroneity.

Despite the propensity for DTW to align excursion nadirs (a hallmark of a least-squares algorithm), the alignments selected for the global Ediacaran $\delta^{\bar{1}3}C_{carb}\text{--Bayesian}$ age model predict a multi-excursion correlation scheme for those excursions generally considered the "BACE" (Fig. 7b). For example, the chosen alignment of the northwest Canada regional composite to the Oman regional composite predicts that the nadir of the CIE in the Risky Formation, Canada, aligns stratigraphically below the nadir of the CIE in the Ara Formation, Oman, such that the former is predicted to have occurred at 544.50 \pm 1.89 Ma while the latter is predicted to have occurred at 540.75 \pm 0.81 Ma. Likewise, the selected DTW alignments between the Great Basin and Mongolia regional composites and the Oman regional composite place the nadirs of the CIEs in the Johnnie Formation and the Zuun Arts Formation stratigraphically higher still, such that these excursions nadirs are predicted to have occurred after the youngest age constraint (< 537.95 \pm 0.53 Ma).

How do these $\delta^{13}C_{carb}$ –Bayesian age model predictions compare to BACE geochronology? The age of synchrony of the BACE remains debated. In Oman, an ash below the onset of the excursion in the Ara Formation was dated to 541.00 \pm 0.13 Ma (Bowring et al., 2007); at Sonora, Mexico, the nadir of the excursion in the La Ciénega Formation

occurs stratigraphically below a maximum depositional age of \leq 539.40 \pm 0.23 Ma (Hodgin et al., 2021). Yet, high-resolution, fossiliferous Ediacaran–Cambrian strata of the Nama Group do not preserve a candidate BACE (Linnemann et al., 2019; Nelson et al., 2022), raising the question of whether the BACE is younger than 538.04 \pm 0.14 Ma, the age of the ash bed at the top of the Nomtsas Formation. If the underlying DTW alignment selections are accurate, then the $\delta^{13}C_{carb}$ –Bayesian age model predicts that the excursions previously attributed to the BACE are asynchronous (Fig. 7b), with excursions at Oman and NW Canada that satisfy the geochronology of Hodgin et al. (2021) as well as excursions at Great Basin, Mongolia, and Iran that satisfy the chronology of Nelson et al. (2022).

Yet, permissible DTW alignments are not unassailable, and the speculation of a diachronous BACE should receive healthy scrutiny. Given the variability of $\delta^{13}C_{carb}$ values in the latest Ediacaran to earliest Cambrian (e.g., Bowyer et al., 2021; Maloof et al., 2010b), it is not surprising that DTW solutions stretch, squeeze and interpolate in a manner that creates sequenced (not stacked) excursions. We cannot exclude that the selection of alternative alignments, alternative targets, and/or parameter selections that changes along a chemostratigraphic section, would generally be more appropriate.

The $\delta^{13}C_{carb}$ -Bayesian age model allows us to consider the redundancy of the $\delta^{13}C_{carb}$ record by asking which intervals of Ediacaran time

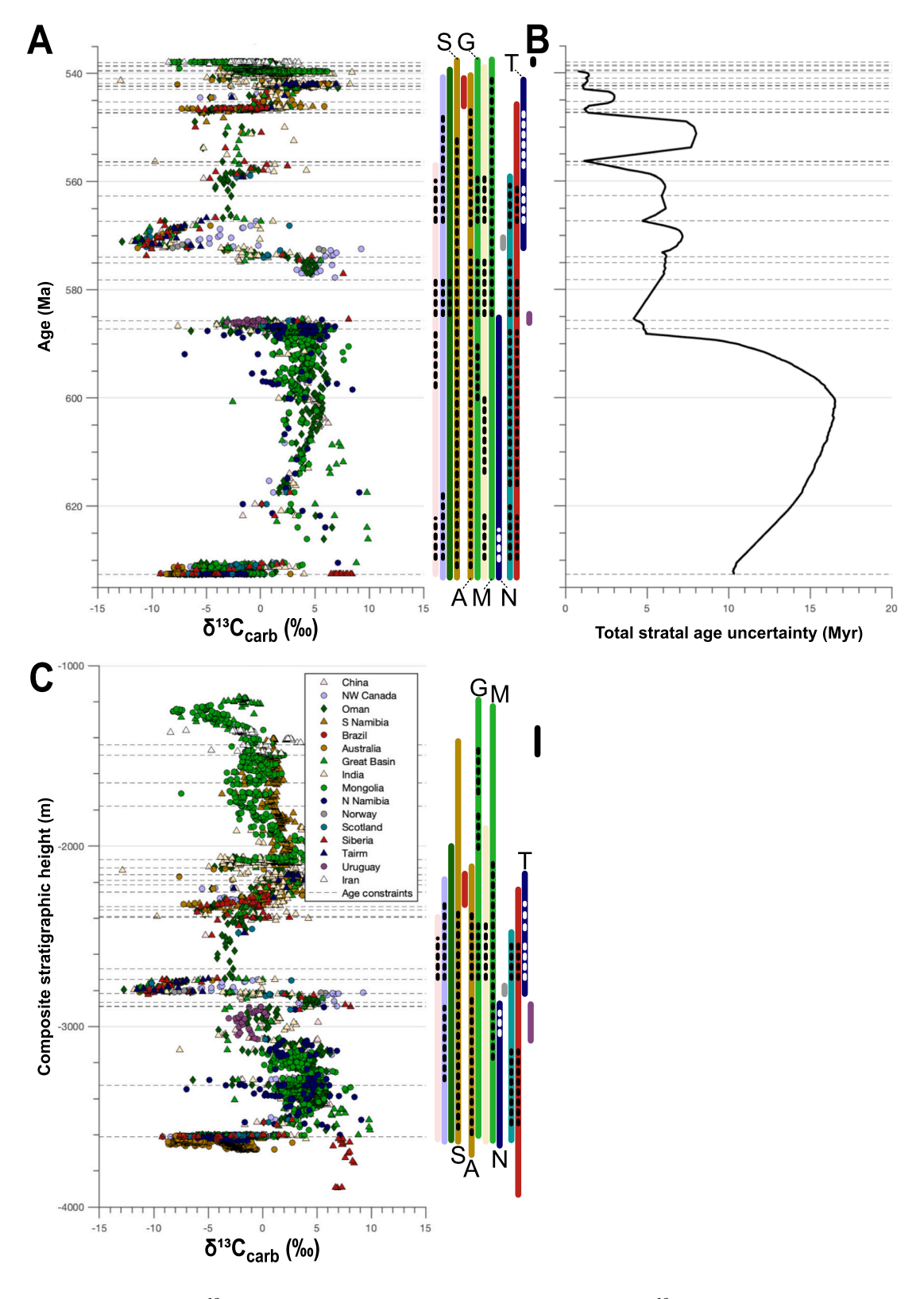


Fig. 6. The DTW-based Ediacaran global $\delta^{13}C_{carb}$ -Bayesian age model. A, the DTW-based Ediacaran global $\delta^{13}C_{carb}$ composite on an age scale according resulting median age from the coupled Bayesian age model and color-coded according to the legend in C. Geochronologic age constraints are shown as dashed black lines. Color-coded bars on the right indicate the temporal extent of deposition in each paleobasin (for the lithostratigraphic units contributed to the underlying $\delta^{13}C_{carb}$ records), with dashed lines indicating intervals of time without a corresponding $\delta^{13}C_{carb}$ record for a given paleobasin, as predicted by the selected alignments. B, total strata age uncertainty (95% confidence interval range) according to Bayesian McMC age model. C, the DTW-based Ediacaran global composite $\delta^{13}C_{carb}$ record on a stratigraphic height scale according to time-calibrated $\delta^{13}C_{carb}$ composite meterage (the Oman target). Color-coded bars on the right indicate the stratigraphic extent of each paleobasin, with dashed lines indicating intervals not captured by deposition in that paleobasin. Acronyms are used when multiple bars are colored the same (differentiated in scatter plots by symbol) and are as follows: S for South Namibia, A for Australia, G for Great Basin, M for Mongolia, N for North Namibia, and T for Tarim.

Table 4
Shuram excursion metrics. The excursion metrics (see text for explanation) for each paleobasin predicted to have a CIE that aligns to the Shuram excursion sensu stricto in the Shuram Formation, Oman regional comosite. N/A indicates that part of the excursion was not recorded in that paleobasin, preventing the calculation of that metric.

Paleobasin	mn (‰)	tn (Myr)	tr (Myr)	Onset age (Ma \pm uncertainty)	Nadir age (Ma \pm uncertainty)	Depletion rate (‰/Myr)
China	14.4	3.98 ± 5.67	3.79 ± 5.83	574.47 ± 3.71	570.49 ± 4.32	3.62
NW Canada	15.9	1.37 ± 5.64	0.62 ± 5.78	572.48 ± 3.71	571.11 ± 4.25	11.61
Oman	17.5	3.51 ± 5.63	4.41 ± 5.78	574.62 ± 3.70	571.11 ± 4.25	4.99
Australia	14.3	0.53 ± 5.59	4.10 ± 5.62	572.75 ± 3.87	572.22 ± 4.03	26.98
Great Basin	16.9	3.96 ± 5.67	3.32 ± 5.82	574.62 ± 3.70	570.66 ± 4.30	4.27
India	14.5	2.03 ± 5.62	2.33 ± 5.78	573.14 ± 3.68	571.11 ± 4.25	7.14
Norway	13.9	0.52 ± 5.59	N/A	572.75 ± 3.87	572.23 ± 4.03	26.73
Scotland	12.3	0.63 ± 5.61	3.96 ± 5.64	572.75 ± 3.87	572.12 ± 4.06	19.52
Siberia	15.4	2.01 ± 5.59	5.11 ± 5.69	573.82 ± 3.76	571.81 ± 4.13	7.66
Tarim	N/A	N/A	4.41 ± 5.78	N/A	571.11 ± 4.25	N/A
Average	15.0	2.06 ± 1.87	3.56 ± 1.92	573.49 ± 3.76	571.40 ± 4.19	12.50

are represented by chemostratigraphic records from one, many, or only a few, paleodepositional regions? For example, the alignment selections predict that long stretches of Ediacaran time between major CIEs—such as from ${\sim}627$ to 622 Ma and ${\sim}566{-}560$ Ma—are represented by deposition at fewer than three (known) paleo-depositional regions. Further, the $\delta^{13}C_{carb}{-}Bayesian$ age model predicts a temporal gap in the Ediacaran $\delta^{13}C_{carb}$ chemostratigraphic record from 585.38 ± 2.57 Ma to 577.87 ± 3.80 Ma. While this prediction may itself be a relict of the choice of Oman for the age model backbone—as the algorithm may not be guiding the insertion of chemostratigraphic records into the time of deposition of the siliciclastic portion of the Khufai Formation—multiple

intervals with low geographic representation raise tantalizing questions about chemostratigraphic representation of the Ediacaran carbonate engine. Notably, the Gaskiers Formation diamictite (the Gaskiers glaciation sensu stricto), while constrained to a sub-million year duration from 580.90 ± 0.40 Ma to 579.88 ± 0.44 Ma (Pu et al., 2016), occurred entirely within this predicted gap in $\delta^{13}C_{carb}$ values. Might this indicate that at late Ediacaran ice age (Wang et al., 2023) temporarily suppressed carbonate production for 7.51 \pm 4.59 Myr? Previous work has also documented unconformities underlying the Shuram excursion in some paleobasins that may help account for this predicted gap in $\delta^{13}C_{carb}$ values (e.g., Fike et al., 2006; Macdonald et al., 2013). While the

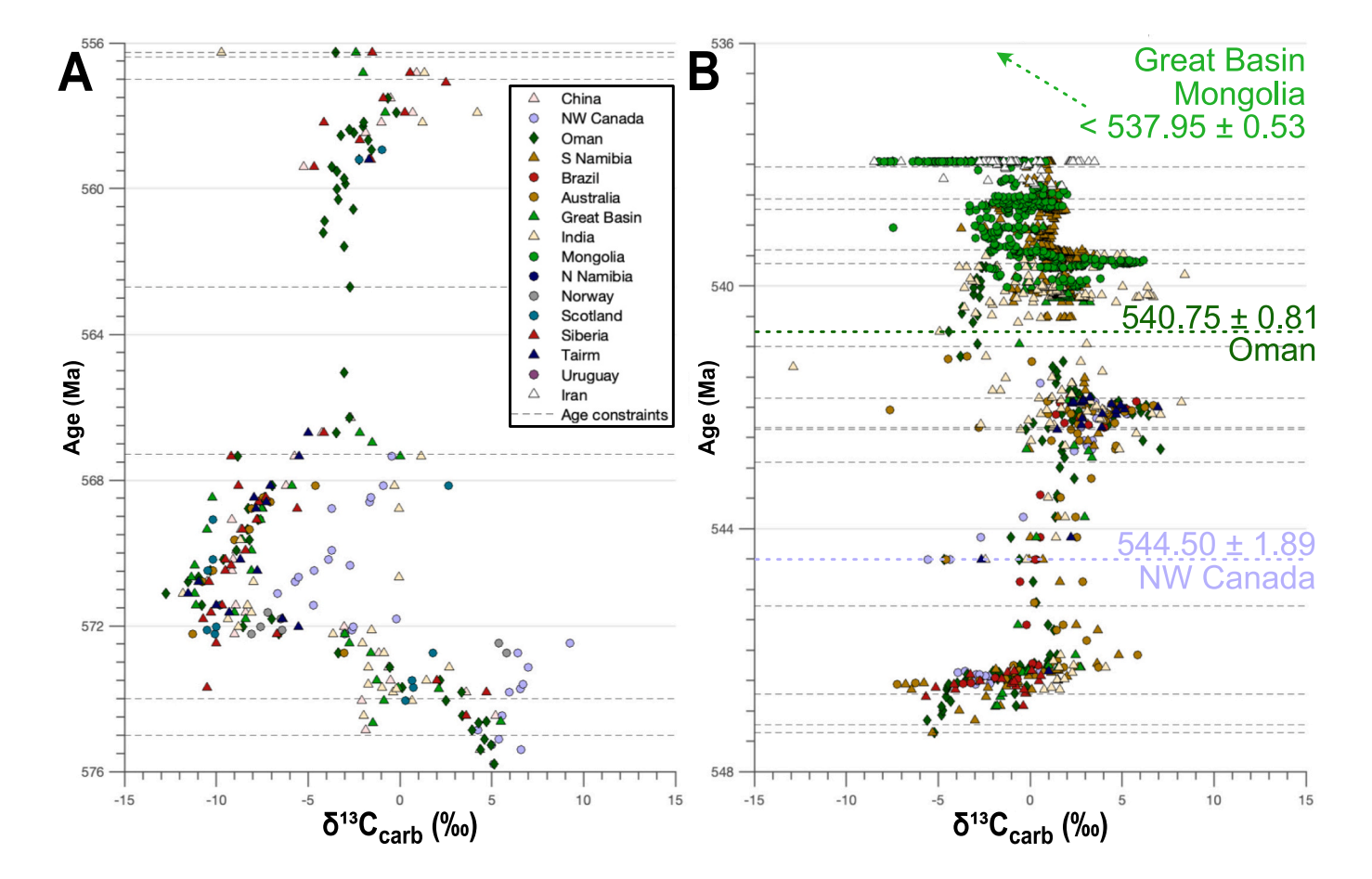


Fig. 7. The Shuram and basal Cambrian excursions as predicted by the DTW-based Ediacaran global $\delta^{13}C_{carb}$ -Bayesian age model. A zoom-in of Fig. 6A to better show the alignment of carbon isotope excursions cited in the literature as A, the Shuram excursion and B, the basal Cambrian excursion (BACE). The position of the BACE nadir in different paleobasins is indicated with color-coded dashed lines and labels. Points in both panels are color-coded according to the legend in A, and geochronologic age constraints are shown as dashed black lines.

reproduction of CIE from globally distributed depositional regions has received much attention, a $\delta^{13}C_{\text{carb}}$ –Bayesian age model allows us to ask similar questions about fidelity and synchrony of the more pedestrian portions of the Ediacaran chemostratigraphic record.

5. Conclusions

Here we bring to bear two algorithmic tools to explore the time history of deposition of global Ediacaran marine successions: a dynamic time warping algorithm for the alignment of Ediacaran carbon isotope records and a Bayesian age model to infer the depositional age, with uncertainty, for each stratum within the algorithmic chemostratigraphic composite. The resulting global Ediacaran $\delta^{13}C_{carb}$ -Bayesian age model presents the point-to-point alignment of 137 chemostratigraphic records from 16 paleo-depositional regions and assigns to each stratum an uncertainty that varies from 10⁰ to 10¹ Myr. At face value, the new global δ¹³C_{carb}–Bayesian age model can further inquiry into key events in the Ediacaran Period. For example, alignment libraries tend to host high performing solutions that align excursions that primary field workers have suggested are the Shuram; in this case, a $\delta^{13}C_{carb}$ -Bayesian age model allows one to speculate on the timing of the local nadir and, for example, develop hypotheses for whether predicted discrepancies arise from stratigraphic incompleteness or excursion asynchrony. In contrast, alignment libraries tend to host solutions that place excursions that have been hypothesized as the basal Cambrian isotopic excursion (BACE) in series (a temporal succession), not in synchrony. Here algorithmic alignment outcomes should not arbitrate over the synchrony of such excursions, but rather generate testable hypotheses as to how many distinct excursions may exist, and which may be correlative (based on minimizing the squared differences of isotopic values), both questions difficult to achieve without mathematical optimization.

Yet, this age model rests upon assumptions that Ediacaran carbon isotope excursions are globally synchronous and affect all carbonates produced at a particular time and that the underlying alignments are accurate and unique. Thus, we envision this age model as a waypoint for future work that explores alternative age models that can arise when incorporating analytical uncertainty in $\delta^{13}C_{carb}$ values; selecting all geologically permissible alignments; and considering permutations arising from alternative target record selection.

CRediT authorship contribution statement

Cedric J. Hagen: Conceptualization, Data curation, Formal analysis, Funding acquisition, Investigation, Methodology, Software, Validation, Visualization, Writing – original draft, Writing – review & editing. **Jessica R. Creveling:** Conceptualization, Funding acquisition, Investigation, Methodology, Project administration, Software, Supervision, Writing – original draft, Writing – review & editing.

Declaration of competing interest

The authors declare that they have no known competing financial interests or personal relationships that could have appeared to influence the work reported in this paper.

Data availability

Data will be made available on request.

Acknowledgements

This work was made possible by National Science Foundation (NSF) grant EAR-2025735, the ARCS Foundation, a NSF Graduate Research Fellowship, and an Agouron Institute Geobiology Postdoctoral Fellowship. We are grateful to: J. Strauss, P. Sadler, G. Halverson, A. Meigs, E. Brook, A. Mix, A. Maloof, R. Mahon, E. Trower, M. Cantine, A. Knoll and

K. Jay for fruitful discussions and feedback; A. Dickson and H. Falcon-Lang for editorial handling; and Lyle Nelson and two anonymous reviewers for comprehensive feedback that greatly improved this contribution.

Appendix A. Supplementary data

Supplementary data to this article can be found online at $\frac{\text{https:}}{\text{doi.}}$ org/10.1016/j.palaeo.2024.112321.

References

- Allen, P.A., Leather, J., Brasier, M.D., 2004. The Neoproterozoic Fiq glaciation and its aftermath, Huqf supergroup of Oman. Basin Res. 16, 507–534. https://doi.org/10.1111/j.1365-2117.2004.00249.x.
- Ansari, A.H., Pandey, S.K., Sharma, M., Agrawal, S., Kumar, Y., 2018. Carbon and oxygen isotope stratigraphy of the Ediacaran Bilara Group, Marwar Supergroup, India: Evidence for high amplitude carbon isotopic negative excursions. Precambrian Res. 308, 75–91. https://doi.org/10.1016/j.precamres.2018.02.002.
- Aubet, N.R., Pecoits, E., Bekker, A., Gingras, M.K., Zwingmann, H., Veroslavsky, G., de Santa Ana, H., Konhauser, K.O., 2012. Chemostratigraphic constraints on early Ediacaran carbonate ramp dynamics, Río de la Plata craton, Uruguay. Gondwana Res. 22, 1073–1090. https://doi.org/10.1016/j.gr.2012.03.011.
- Bagnoud-Velásquez, M., Spangenberg, J.E., Poiré, D.G., Gómez Peral, L.E., 2013. Stable isotope (S, C) chemostratigraphy and hydrocarbon biomarkers in the Ediacaran upper section of Sierras Bayas Group, Argentina. Precambrian Res. 231, 388–400. https://doi.org/10.1016/j.precamres.2013.04.001.
- Basei, M.A.S., Drukas, C.O., Nutman, A.P., Wemmer, K., Dunyi, L., Santos, P.R., Passarelli, C.R., Campos Neto, M.C., Siga, O., Osako, L., 2011. The Itajaf foreland basin: a tectono-sedimentary record of the Ediacaran period, Southern Brazil. Int. J. Earth Sci. (Geol Rundsch) 100, 543–569. https://doi.org/10.1007/s00531-010-0604-4
- Beasecker, J., Chamberlin, Z., Lane, N., Reynolds, K., Stack, J., Wahrer, K., Wolff, A., Devilbliss, J., Wahr, C., Durbin, D., Garneau, H., Brandt, D., 2020. It's time to defuse the Cambrian "Explosion". GSAT 30, 26–27. https://doi.org/10.1130/ GSATC460GW 1
- Bergmann, K.D., Zentmyer, R.A., Fischer, W.W., 2011. The stratigraphic expression of a large negative carbon isotope excursion from the Ediacaran Johnnie Formation, Death Valley. Precambrian Res. 188, 45–56. https://doi.org/10.1016/j. precamres.2011.03.014.
- Bjerrum, C.J., Canfield, D.E., 2011. Towards a quantitative understanding of the late Neoproterozoic carbon cycle. Proc. Natl. Acad. Sci. 108, 5542–5547. https://doi. org/10.1073/pnas.1101755108.
- Boggiani, P.C., Gaucher, C., Sial, A.N., Babinski, M., Simon, C.M., Riccomini, C., Ferreira, V.P., Fairchild, T.R., 2010. Chemostratigraphy of the Tamengo Formation (Corumbá Group, Brazil): A contribution to the calibration of the Ediacaran carbonisotope curve. Precambrian Res., Precambrian Isotope Stratigraphy 182, 382–401. https://doi.org/10.1016/j.precamres.2010.06.003.
- Bold, U., Smith, E.F., Rooney, A.D., Bowring, S.A., Buchwaldt, R., Dudás, F.Ö., Ramezani, J., Crowley, J.L., Schrag, D.P., Macdonald, F.A., 2016. Neoproterozoic stratigraphy of the Zavkhan terrane of Mongolia: The backbone for Cryogenian and early Ediacaran chemostratigraphic records. Am. J. Sci. 316, 1–63. https://doi.org/ 10.2475/01.2016.01.
- Bowring, S.A., Grotzinger, J.P., Isachsen, C.E., Knoll, A.H., Pelechaty, S.M., Kolosov, P., 1993. Calibrating rates of early Cambrian evolution. Science 261, 1293–1298. https://doi.org/10.1126/science.11539488.
- Bowring, S.A., Grotzinger, J.P., Condon, D.J., Ramezani, J., Newall, M.J., Allen, P.A., 2007. Geochronologic constraints on the chronostratigraphic framework of the Neoproterozoic Huqf Supergroup, Sultanate of Oman. Am. J. Sci. 307, 1097–1145. https://doi.org/10.2475/10.2007.01.
- Bowyer, F.T., Zhuravlev, A.Y., Wood, R., Shields, G.A., Zhou, Y., Curtis, A., Poulton, S. W., Condon, D.J., Yang, C., Zhu, M., 2021. Calibrating the temporal and spatial dynamics of the Ediacaran Cambrian radiation of animals. Earth Sci. Rev. 103913 https://doi.org/10.1016/j.earscirev.2021.103913.
- Bristow, T.F., Kennedy, M.J., 2008. Carbon isotope excursions and the oxidant budget of the Ediacaran atmosphere and ocean. Geology 36, 863–866. https://doi.org/ 10.1130/G24968A.1.
- Burns, S.J., Matter, A., 1993. Carbon isotopic record of the latest Proterozoic from Oman. Eclogae Geol. Helv. 86. 595–607.
- Busch, J.F., Hodgin, E.B., Ahm, A.-S.C., Husson, J.M., Macdonald, F.A., Bergmann, K.D., Higgins, J.A., Strauss, J.V., 2022. Global and local drivers of the Ediacaran Shuram carbon isotope excursion. Earth Planet. Sci. Lett. 579, 117368 https://doi.org/ 10.1016/j.epsl.2022.117368.
- Calver, C.R., 2000. Isotope stratigraphy of the Ediacarian (Neoproterozoic III) of the Adelaide Rift Complex, Australia, and the overprint of water column stratification. Precambrian Res. 100, 121–150. https://doi.org/10.1016/S0301-9268(99)00072-8.
- Canfield, D.E., Knoll, A.H., Poulton, S.W., Narbonne, G.M., Dunning, G.R., 2020. Carbon isotopes in clastic rocks and the Neoproterozoic carbon cycle. Am. J. Sci. 320, 97–124
- Chen, C., Feng, Q., Gan, Z., 2020. Zircon U-Pb ages and its geological significance of tuffs between Doushantuo and Liuchapo formations at Yangtou Section, Guizhou Province. Earth Sci. 45, 880–891.

- Chen, X., Zhou, P., Zhang, B., Wang, C., 2015. Stable isotope records of the Ediacaran Doushantuo Formation in the eastern Yangtze Gorges and its significance for choronostratigraphy. Geol. China 42, 207–223.
- Cohen, K.M., Finney, S.C., Gibbard, P.L., Fan, J.-X., 2013. The ICS international chronostratigraphic chart. Episod. J. Int. Geosci. 36, 199–204.
- Condon, D., Zhu, M., Bowring, S., Wang, W., Yang, A., Jin, Y., 2005. U-Pb Ages from the Neoproterozoic Doushantuo Formation, China. Science 308, 95–98. https://doi.org/ 10.1126/science.1107765
- Corsetti, F.A., Kaufman, A.J., 2003. Stratigraphic investigations of carbon isotope anomalies and Neoproterozoic ice ages in Death Valley, California. GSA Bull. 115, 916–932. https://doi.org/10.1130/B25066.1.
- Creveling, J.R., Bergmann, K.D., Grotzinger, J.P., 2016. Cap carbonate platform facies model, Noonday Formation, SE California. GSA Bull. 128, 1249–1269. https://doi. org/10.1130/B31442.1.
- Cui, H., Grazhdankin, D.V., Xiao, S., Peek, S., Rogov, V.I., Bykova, N.V., Sievers, N.E., Liu, X.-M., Kaufman, A.J., 2016. Redox-dependent distribution of early macroorganisms: Evidence from the terminal Ediacaran Khatyspyt Formation in Arctic Siberia. Palaeogeogr. Palaeoclimatol. Palaeoecol. 461, 122–139. https://doi.org/ 10.1016/j.palaeo.2016.08.015.
- Cui, H., Kaufman, A.J., Xiao, S., Zhou, C., Liu, X.-M., 2017. Was the Ediacaran Shuram Excursion a globally synchronized early diagenetic event? Insights from methanederived authigenic carbonates in the uppermost Doushantuo Formation, South China. Chem. Geol. 450, 59–80. https://doi.org/10.1016/j.chemgeo.2016.12.010.
- Cui, H., Kaufman, A.J., Peng, Y., Liu, X.-M., Plummer, R.E., Lee, E.I., 2018. The Neoproterozoic Hüttenberg 613C anomaly: Genesis and global implications. Precambrian Res. 313, 242–262. https://doi.org/10.1016/j.precamres.2018.05.024.
- Derry, L.A., 2010. A burial diagenesis origin for the Ediacaran Shuram—Wonoka carbon isotope anomaly. Earth Planet. Sci. Lett. 294, 152–162. https://doi.org/10.1016/j. epsl.2010.03.022.
- Droser, M.L., Gehling, J.G., 2015. The advent of animals: The view from the Ediacaran. Proc. Natl. Acad. Sci. 112, 4865–4870. https://doi.org/10.1073/pnas.1403669112.
- Erwin, D.H., Laflamme, M., Tweedt, S.M., Sperling, E.A., Pisani, D., Peterson, K.J., 2011. The Cambrian Conundrum: Early Divergence and Later Ecological Success in the Early History of Animals. Science 334, 1091–1097. https://doi.org/10.1126/ science 1206375
- Etemad-Saeed, N., Knoll, A.H., Najafi, M., Bergmann, K.D., Haseley, N., Karimi, S., 2021. Carbon isotope chemostratigraphy of a Gondwanan Ediacaran–Cambrian transition, Soltanieh Mountains, northern Iran. Gondwana Res. 99, 163–177. https://doi.org/ 10.1016/j.gr.2021.07.001.
- Fike, D.A., Grotzinger, J.P., 2008. A paired sulfate–pyrite 834S approach to understanding the evolution of the Ediacaran–Cambrian sulfur cycle. Geochim. Cosmochim. Acta 72, 2636–2648. https://doi.org/10.1016/j.gca.2008.03.021.
- Fike, D.A., Grotzinger, J.P., Pratt, L.M., Summons, R.E., 2006. Oxidation of the Ediacaran Ocean. Nature 444, 744–747. https://doi.org/10.1038/nature05345.
- Grazhdankin, D.V., Marusin, V.V., Meert, J., Krupenin, M.T., Maslov, A.V., 2011. Kotlin regional stage in the South Urals. Dokl. Earth Sc. 440, 1222–1226. https://doi.org/ 10.1134/S1028334X11090170.
- Grotzinger, J.P., Fike, D.A., Fischer, W.W., 2011. Enigmatic origin of the largest-known carbon isotope excursion in Earth's history. Nat. Geosci. 4, 285–292. https://doi. org/10.1038/ngeo1138.
- Haam, E., Huybers, P., 2010. A test for the presence of covariance between timeuncertain series of data with application to the Dongge Cave speleothem and atmospheric radiocarbon records. Paleoceanography 25. https://doi.org/10.1029/ 2008PA001713.
- Hagen, C.J., Creveling, J.R., Huybers, P., 2024. Align: A User-Friendly App for Numerical Stratigraphic Correlation. GSA Today 34, 4–9. https://doi.org/10.1130/ GSATG575A.1.
- Halverson, G.P., Hoffman, P.F., Schrag, D.P., Maloof, A.C., Rice, A.H.N., 2005. Toward a Neoproterozoic composite carbon-isotope record. GSA Bull. 117, 1181–1207. https://doi.org/10.1130/B25630.1.
- Haslett, J., Parnell, A., 2008. A simple monotone process with application to radiocarbon-dated depth chronologies. J. R. Stat. Soc.: Ser. C: Appl. Stat. 57, 399–418. https://doi.org/10.1111/j.1467-9876.2008.00623.x.
- Hay, C.C., Creveling, J.R., Hagen, C.J., Maloof, A.C., Huybers, P., 2019. A library of early Cambrian chemostratigraphic correlations from a reproducible algorithm. Geology 47, 457–460. https://doi.org/10.1130/G46019.1.
- Hodgin, E.B., Nelson, L.L., Wall, C.J., Barrón-Díaz, A.J., Webb, L.C., Schmitz, M.D., Fike, D.A., Hagadorn, J.W., Smith, E.F., 2021. A link between rift-related volcanism and end-Ediacaran extinction? Integrated chemostratigraphy, biostratigraphy, and U-Pb geochronology from Sonora, Mexico. Geology 49, 115–119. https://doi.org/ 10.1130/G47972.1.
- Hoffman, P.F., Lamothe, K.G., 2019. Seawater-buffered diagenesis, destruction of carbon isotope excursions, and the composition of DIC in Neoproterozoic oceans. PNAS 116, 18874–18879. https://doi.org/10.1073/pnas.1909570116.
- Hoffman, P.F., Li, Z.-X., 2009. A palaeogeographic context for Neoproterozoic glaciation. Palaeogeogr. Palaeoclimatol. Palaeoecol. 277, 158–172. https://doi.org/10.1016/j.palaeo.2009.03.013.
- Hoffman, P.F., Kaufman, A.J., Halverson, G.P., Schrag, D.P., 1998. A neoproterozoic snowball earth. Science 281, 1342–1346. https://doi.org/10.1126/ science.281.5381.1342.
- Huang, T., Chen, D., Ding, Y., Zhou, X., Zhang, G., 2020. SIMS U-Pb Zircon Geochronological and Carbon Isotope Chemostratigraphic Constraints on the Ediacaran-Cambrian Boundary Succession in the Three Gorges Area, South China. J. Earth Sci. 31, 69–78. https://doi.org/10.1007/s12583-019-1233-x.

- Husson, J.M., Maloof, A.C., Schoene, B., Chen, C.Y., Higgins, J.A., 2015. Stratigraphic expression of Earth's deepest $\delta 13C$ excursion in the Wonoka Formation of South Australia. Am. J. Sci. 315, 1–45. https://doi.org/10.2475/01.2015.01.
- Jiang, G., Kaufman, A.J., Christie-Blick, N., Zhang, S., Wu, H., 2007. Carbon isotope variability across the Ediacaran Yangtze platform in South China: Implications for a large surface-to-deep ocean 813C gradient. Earth Planet. Sci. Lett. 261, 303–320. https://doi.org/10.1016/j.epsl.2007.07.009.
- Johnston, D.T., Macdonald, F.A., Gill, B.C., Hoffman, P.F., Schrag, D.P., 2012. Uncovering the Neoproterozoic carbon cycle. Nature 483, 320–323. https://doi.org/ 10.1038/nature10854.
- Kaufman, A.J., Knoll, A.H., 1995. Neoproterozoic variations in the C-isotopic composition of seawater: stratigraphic and biogeochemical implications. In: Precambrian Research, Neoproterozoic Stratigraphy and Earth History, 73, pp. 27–49. https://doi.org/10.1016/0301-9268(94)00070-8.
- Kaufman, A.J., Jiang, G., Christie-Blick, N., Banerjee, D.M., Rai, V., 2006. Stable isotope record of the terminal Neoproterozoic Krol platform in the Lesser Himalayas of northern India. Precambrian Res. 147, 156–185. https://doi.org/10.1016/j. precamps 2006.02.007
- Kaufman, A.J., Corsetti, F.A., Varni, M.A., 2007. The effect of rising atmospheric oxygen on carbon and sulfur isotope anomalies in the Neoproterozoic Johnnie Formation, Death Valley, USA. Chem. Geolo., Precambr. Chemostratigraph. 237, 47–63. https:// doi.org/10.1016/j.chemgeo.2006.06.023.
- Kirschvink, J.L., 1992. Late Proterozoic Low-Latitude Global Glaciation: the Snowball Earth. In: The Proterozoic Biosphere: A Multidisciplinary Study. Cambridge University Press, New York, pp. 51–52.
- Knoll, A.H., Hayes, J.M., Kaufman, A.J., Swett, K., Lambert, I.B., 1986. Secular variation in carbon isotope ratios from Upper Proterozoic successions of Svalbard and East Greenland. Nature 321, 832–838. https://doi.org/10.1038/321832a0.
- Knoll, A., Walter, M., Narbonne, G., Christie-Blick, N., 2006. The Ediacaran Period: a new addition to the geologic time scale. Lethaia 39, 13–30. https://doi.org/10.1080/ 00241160500409223.
- Landing, E., Schmitz, M.D., Geyer, G., Trayler, R.B., Bowring, S.A., 2021. Precise early Cambrian U–Pb zircon dates bracket the oldest trilobites and archaeocyaths in Moroccan West Gondwana. Geol. Mag. 158, 219–238. https://doi.org/10.1017/ S0016756820000369.
- Li, C., Planavsky, N.J., Shi, W., Zhang, Z., Zhou, C., Cheng, M., Tarhan, L.G., Luo, G., Xie, S., 2015. Ediacaran Marine Redox Heterogeneity and Early Animal Ecosystems. Sci. Rep. 5, 17097. https://doi.org/10.1038/srep17097.
- Linnemann, U., Ovtcharova, M., Schaltegger, U., Gärtner, A., Hautmann, M., Geyer, G., Vickers-Rich, P., Rich, T., Plessen, B., Hofmann, M., Zieger, J., Krause, R., Kriesfeld, L., Smith, J., 2019. New high-resolution age data from the Ediacaran–Cambrian boundary indicate rapid, ecologically driven onset of the Cambrian explosion. Terra Nova 31, 49–58. https://doi.org/10.1111/ter.12368.
- Lisiecki, L.E., Lisiecki, P.A., 2002. Application of dynamic programming to the correlation of paleoclimate records. Paleoceanography 17. https://doi.org/10.1029/ 2001PA000733, 1-1-1-12.
- Lisiecki, L.E., Raymo, M.E., 2005. A Pliocene-Pleistocene stack of 57 globally distributed benthic δ18O records. Paleoceanography 20. https://doi.org/10.1029/
- Liu, P., Yin, C., Gao, L., Tang, F., Chen, S., 2009. New material of microfossils from the Ediacaran Doushantuo Formation in the Zhangcunping area, Yichang, Hubei Province and its zircon SHRIMP U-Pb age. Chin. Sci. Bull. 54, 1058–1064. https://doi.org/10.1007/s11434-008-0589-6
- Llanos, M.P.I., Tait, J.A., Popov, V., Abalmassova, A., 2005. Palaeomagnetic data from Ediacaran (Vendian) sediments of the Arkhangelsk region, NW Russia: An alternative apparent polar wander path of Baltica for the Late Proterozoic–Early Palaeozoic. Earth Planet. Sci. Lett. 240, 732–747. https://doi.org/10.1016/j.epsl.2005.09.063.
- Loyd, S.J., Marenco, P.J., Hagadorn, J.W., Lyons, T.W., Kaufman, A.J., Sour-Tovar, F., Corsetti, F.A., 2012. Sustained low marine sulfate concentrations from the Neoproterozoic to the Cambrian: Insights from carbonates of northwestern Mexico and eastern California. Earth Planet. Sci. Lett. 339–340, 79–94. https://doi.org/ 10.1016/j.epsl.2012.05.032.
- Macdonald, Francis A., Strauss, J.V., Rose, C.V., Dudás, F.H.O., Schrag, D.P., 2010.
 Stratigraphy of the Port Nolloth Group of Namibia and South Africa and implications for the age of Neoproterozoic iron formations. Am. J. Sci. 310, 862–888.
- Macdonald, F.A., Strauss, J.V., Sperling, E.A., Halverson, G.P., Narbonne, G.M., Johnston, D.T., Kunzmann, M., Schrag, D.P., Higgins, J.A., 2013. The stratigraphic relationship between the Shuram carbon isotope excursion, the oxygenation of Neoproterozoic oceans, and the first appearance of the Ediacara biota and bilaterian trace fossils in northwestern Canada. Chem. Geol. 362, 250–272. https://doi.org/10.1016/j.chemgeo.2013.05.032. Special Issue dedicated to H.D. Holland: Evolution of the atmosphere and ocean through time.
- Maloof, A.C., Porter, S.M., Moore, J.L., Dudás, F.Ö., Bowring, S.A., Higgins, J.A., Fike, D. A., Eddy, M.P., 2010a. The earliest Cambrian record of animals and ocean geochemical change. GSA Bull. 122, 1731–1774. https://doi.org/10.1130/ B20246.1
- Maloof, A.C., Ramezani, J., Bowring, S.A., Fike, D.A., Porter, S.M., Mazouad, M., 2010b. Constraints on early Cambrian carbon cycling from the duration of the Nemakit-Daldynian-Tommotian boundary δ13C shift, Morocco. Geology 38, 623–626. https://doi.org/10.1130/G30726.1.
- Marshall, C.R., 2006. Explaining the Cambrian "Explosion" of Animals. Annu. Rev. Earth Planet. Sci. 34, 355–384. https://doi.org/10.1146/annurev. earth.33.031504.103001.
- Matthews, J.J., Liu, A.G., Yang, C., McIlroy, D., Levell, B., Condon, D.J., 2020.

 A chronostratigraphic framework for the rise of the ediacaran macrobiota: New

- constraints from mistaken point ecological reserve, Newfoundland. GSA Bull. 133, 612-624. https://doi.org/10.1130/B35646.1.
- Melezhik, V.A., Roberts, D., Fallick, A.E., Gorokhov, I.M., 2008. The Shuram–Wonoka event recorded in a high-grade metamorphic terrane: insight from the Scandinavian Caledonides. Geol. Mag. 145 https://doi.org/10.1017/S0016756807004189.
- Melezhik, V.A., Pokrovsky, B.G., Fallick, A.E., Kuznetsov, A.B., Bujakaite, M.I., 2009. Constraints on 875r/86Sr of Late Ediacaran seawater: insight from Siberian high-Sr limestones. J. Geol. Soc. Lond. 166, 183–191. https://doi.org/10.1144/0016-76492007-171
- Morris, S.C., 1993. The fossil record and the early evolution of the Metazoa. Nature 361, 219–225. https://doi.org/10.1038/361219a0.
- Narbonne, G.M., 2005. The Ediacara Biota: Neoproterozoic Origin of Animals and Their Ecosystems. Annu. Rev. Earth Planet. Sci. 33, 421–442. https://doi.org/10.1146/ annurev.earth.33.092203.122519.
- Narbonne, G.M., Gehling, J.G., 2003. Life after snowball: The oldest complex Ediacaran fossils. Geology 31, 27–30. https://doi.org/10.1130/0091-7613(2003)031<0027: LASTOC>2.0 CO:2
- Narbonne, G.M., Xiao, S., Shields, G.A., Gehling, J.G., 2012. The Ediacaran period. In: The Geologic Time Scale 2012. Elsevier, pp. 413–435. https://doi.org/10.1016/B978-0-444-59425-9.00018-4.
- Nelson, L.L., Crowley, J.L., Smith, E.F., Schwartz, D.M., Hodgin, E.B., Schmitz, M.D., 2023. Cambrian explosion condensed: High-precision geochronology of the lower Wood Canyon Formation, Nevada. Proc. Natl. Acad. Sci. 120, e2301478120 https://doi.org/10.1073/pnas.2301478120.
- Nelson, L.L., Ramezani, J., Almond, J.E., Darroch, S.A.F., Taylor, W.L., Brenner, D.C., Furey, R.P., Turner, M., Smith, E.F., 2022. Pushing the boundary: A calibrated Ediacaran-Cambrian stratigraphic record from the Nama Group in northwestern Republic of South Africa. Earth Planet. Sci. Lett. 580, 117396 https://doi.org/ 10.1016/j.epsl.2022.117396.
- Noble, S.R., Condon, D.J., Carney, J.N., Wilby, P.R., Pharaoh, T.C., Ford, T.D., 2015. U-Pb geochronology and global context of the Charnian Supergroup, UK: Constraints on the age of key Ediacaran fossil assemblages. GSA Bull. 127, 250–265. https://doi.org/10.1130/B31013.1.
- Osburn, M.R., Owens, J., Bergmann, K.D., Lyons, T.W., Grotzinger, J.P., 2015. Dynamic changes in sulfate sulfur isotopes preceding the Ediacaran Shuram Excursion. Geochim. Cosmochim. Acta 170, 204–224. https://doi.org/10.1016/j.gca.2015.07.039.
- Parry, L.A., Boggiani, P.C., Condon, D.J., Garwood, R.J., Leme, J. de M., McIlroy, D., Brasier, M.D., Trindade, R., Campanha, G.A.C., Pacheco, M.L.A.F., Diniz, C.Q.C., Liu, A.G., 2017. Ichnological evidence for meiofaunal bilaterians from the terminal Ediacaran and earliest Cambrian of Brazil. Nat. Ecol. Evol. 1, 1455–1464. https:// doi.org/10.1038/s41559-017-0301-9.
- Paulsen, T., Deering, C., Sliwinski, J., Bachmann, O., Guillong, M., 2017. Evidence for a spike in mantle carbon outgassing during the Ediacaran period. Nat. Geosci. 10, 930–934. https://doi.org/10.1038/s41561-017-0011-6.
- Petterson, R., Prave, A.R., Wernicke, B.P., Fallick, A.E., 2011. The Neoproterozoic Noonday Formation, Death Valley region, California. GSA Bull. 123, 1317–1336. https://doi.org/10.1130/B30281.1.
- Pokrovskii, B.G., Melezhik, V.A., Bujakaite, M.I., 2006. Carbon, oxygen, strontium, and sulfur isotopic compositions in late Precambrian rocks of the Patom Complex, central Siberia: Communication 1. results, isotope stratigraphy, and dating problems. Lithol. Miner. Resour. 41, 450–474. https://doi.org/10.1134/S0024490206050063.
- Porter, S.M., 2004. The fossil record of early eukaryotic diversification. Paleontol. Soc. pap. 10, 35–50. https://doi.org/10.1017/S1089332600002321.
- Porter, S.M., Knoll, A.H., Affaton, P., 2004. Chemostratigraphy of Neoproterozoic cap carbonates from the Volta Basin, West Africa. Precambrian Res. 130, 99–112. https://doi.org/10.1016/j.precamres.2003.10.015.
- Prave, A.R., 1999. Two diamictites, two cap carbonates, two δ13C excursions, two rifts: The Neoproterozoic Kingston Peak Formation, Death Valley, California. Geology 27, 339–342. https://doi.org/10.1130/0091-7613(1999)027<0339:TDTCCT>2.3.CO;2.
- Prave, A.R., Fallick, A.E., Thomas, C.W., Graham, C.M., 2009. A composite C-isotope profile for the Neoproterozoic Dalradian Supergroup of Scotland and Ireland. J. Geol. Soc. Lond. 166, 845–857. https://doi.org/10.1144/0016-76492008-131.
- Prave, A.R., Condon, D.J., Hoffmann, K.H., Tapster, S., Fallick, A.E., 2016. Duration and nature of the end-Cryogenian (Marinoan) glaciation. Geology 44, 631–634. https://doi.org/10.1130/G38089.1.
- Pu, J.P., Bowring, S.A., Ramezani, J., Myrow, P., Raub, T.D., Landing, E., Mills, A., Hodgin, E., Macdonald, F.A., 2016. Dodging snowballs: Geochronology of the Gaskiers glaciation and the first appearance of the Ediacaran biota. Geology 44, 955–958. https://doi.org/10.1130/G38284.1.
- Rooney, A.D., Strauss, J.V., Brandon, A.D., Macdonald, F.A., 2015. A Cryogenian chronology: Two long-lasting synchronous Neoproterozoic glaciations. Geology 43, 459–462. https://doi.org/10.1130/G36511.1.
- Rooney, A.D., Cantine, M.D., Bergmann, K.D., Gómez-Pérez, I., Baloushi, B.A., Boag, T. H., Busch, J.F., Sperling, E.A., Strauss, J.V., 2020. Calibrating the coevolution of Ediacaran life and environment. PNAS 117, 16824–16830. https://doi.org/10.1073/
- Rose, C.V., Maloof, A.C., 2010. Testing models for post-glacial 'cap dolostone' deposition: Nuccaleena Formation, South Australia. Earth Planet. Sci. Lett. 296, 165–180. https://doi.org/10.1016/j.epsl.2010.03.031.
- Rothman, D.H., Hayes, J.M., Summons, R.E., 2003. Dynamics of the Neoproterozoic carbon cycle. PNAS 100, 8124–8129. https://doi.org/10.1073/pnas.0832439100.
- Sahoo, S.K., Planavsky, N.J., Jiang, G., Kendall, B., Owens, J.D., Wang, X., Shi, X., Anbar, A.D., Lyons, T.W., 2016. Oceanic oxygenation events in the anoxic Ediacaran ocean. Geobiology 14, 457–468. https://doi.org/10.1111/gbi.12182.

- Sakoe, H., Chiba, S., 1978. Dynamic programming algorithm optimization for spoken word recognition. IEEE Trans. Acoust. Speech Signal Process. 26, 43–49. https://doi. org/10.1109/TASSP.1978.1163055.
- Saltzman, M.R., 2005. Phosphorus, nitrogen, and the redox evolution of the Paleozoic oceans. Geology 33, 573–576. https://doi.org/10.1130/G21535.1.
- Saylor, B.Z., Kaufman, A.J., Grotzinger, J.P., Urban, F., 1998. A composite reference section for terminal Proterozoic strata of southern Namibia. J. Sediment. Res. 68, 1223–1235. https://doi.org/10.2110/jsr.68.1223.
- Schoene, B., Eddy, M.P., Samperton, K.M., Keller, C.B., Keller, G., Adatte, T., Khadri, S.F. R., 2019. U-Pb constraints on pulsed eruption of the Deccan Traps across the end-Cretaceous mass extinction. Science 363, 862–866. https://doi.org/10.1126/science.aau2422.
- Scholle, P.A., Arthur, M.A., 1980. Carbon Isotope Fluctuations in Cretaceous Pelagic Limestones: Potential Stratigraphic and Petroleum Exploration Tool. AAPG Bull. 64, 67, 97
- Schrag, D.P., Higgins, J.A., Macdonald, F.A., Johnston, D.T., 2013. Authigenic Carbonate and the History of the Global Carbon Cycle. Science 339, 540–543. https://doi.org/ 10.1126/science.1229578.
- Shields, G.A., Mills, B.J.W., Zhu, M., Raub, T.D., Daines, S.J., Lenton, T.M., 2019. Unique Neoproterozoic carbon isotope excursions sustained by coupled evaporite dissolution and pyrite burial. Nat. Geosci. 12, 823–827. https://doi.org/10.1038/ s41561-019-0434-3.
- Smith, Emily F., Macdonald, F.A., Petach, T.A., Bold, U., Schrag, D.P., 2016a. Integrated stratigraphic, geochemical, and paleontological late Ediacaran to early Cambrian records from southwestern Mongolia. GSA Bull. 128, 442–468. https://doi.org/ 10.1130/B31248.1
- Smith, E.F., Nelson, L.L., Strange, M.A., Eyster, A.E., Rowland, S.M., Schrag, D.P., Macdonald, F.A., 2016b. The end of the Ediacaran: Two new exceptionally preserved body fossil assemblages from Mount Dunfee, Nevada, USA. Geology 44, 911–914. https://doi.org/10.1130/G38157.1.
- Soldatenko, Y., El Albani, A., Ruzina, M., Fontaine, C., Nesterovsky, V., Paquette, J.-L., Meunier, A., Ovtcharova, M., 2019. Precise U-Pb age constrains on the Ediacaran biota in Podolia, East European Platform, Ukraine. Sci. Rep. 9, 1675. https://doi. org/10.1038/s41598-018-38448-9.
- Sperling, E.A., Wolock, C.J., Morgan, A.S., Gill, B.C., Kunzmann, M., Halverson, G.P., Macdonald, F.A., Knoll, A.H., Johnston, D.T., 2015. Statistical analysis of iron geochemical data suggests limited late Proterozoic oxygenation. Nature 523, 451-454. https://doi.org/10.1038/nature14589.
- Summa, C.L., 1993. Sedimentologic, stratigraphic, and tectonic controls of a mixed carbonate-siliciclastic succession: Neoproterozoic Johnnie Formation, southeast California. Massachusetts Institute of Technology, Cambridge, Massachusetts.
- Trayler, R.B., Schmitz, M.D., Cuitiño, J.I., Kohn, M.J., Bargo, M.S., Kay, R.F., Strömberg, C.A.E., Vizcaíno, S.F., 2019. An improved approach to age-modeling in deep time: Implications for the Santa Cruz Formation, Argentina. GSA Bull. 132, 233–244. https://doi.org/10.1130/B35203.1.
- Verdel, C., Campbell, M., 2017. Neoproterozoic carbon isotope stratigraphy of the Amadeus Basin, central Australia. GSA Bull. 129, 1280–1299. https://doi.org/ 10.1130/B31562.1.
- Wang, Y., Chen, D., Liu, M., Liu, K., Tang, P., 2022. Ediacaran carbon cycling and Shuram excursion recorded in the Tarim Block, northwestern China. Precambrian Res. 377, 106694 https://doi.org/10.1016/j.precamres.2022.106694.
- Wang, R., Yin, Z., Shen, B., 2023. A late Ediacaran ice age: The key node in the Earth system evolution. Earth Sci. Rev. 247, 104610 https://doi.org/10.1016/j. earscirev.2023.104610.
- Wood, R.A., Poulton, S.W., Prave, A.R., Hoffmann, K.-H., Clarkson, M.O., Guilbaud, R., Lyne, J.W., Tostevin, R., Bowyer, F., Penny, A.M., Curtis, A., Kasemann, S.A., 2015. Dynamic redox conditions control late Ediacaran metazoan ecosystems in the Nama Group, Namibia. Precambrian Res. 261, 252–271. https://doi.org/10.1016/j.precamres.2015.02.004.
- Xiao, S., Narbonne, G.M., Zhou, C., Laflamme, M., Grazhdankin, D.V., Moczydlowska-Vidal, M., Cui, H., 2016. Towards an Ediacaran Time Scale: Problems, Protocols, and Prospects. Episodes 39, 540–555. https://doi.org/10.18814/epiiugs/2016/v39i4/103886.
- Yang, H., Hu, A., Zheng, J., Liang, F., Luo, X., Feng, Y., Shen, A., 2020. Application of mapping and dating techniques in the study of ancient carbonate reservoirs: A case study of Sinian Qigebrak Formation in northwestern Tarim Basin, NW China. Pet. Explor. Dev. 47, 1001–1013. https://doi.org/10.1016/S1876-3804(20)60112-4.
- Yang, C., Li, X.-H., Zhu, M., Condon, D.J., 2017. SIMS U-Pb zircon geochronological constraints on upper Ediacaran stratigraphic correlations, South China. Geol. Mag. 154, 1202–1216. https://doi.org/10.1017/S0016756816001102.
- Yang, C., Rooney, A.D., Condon, D.J., Li, X.-H., Grazhdankin, D.V., Bowyer, F.T., Hu, C., Macdonald, F.A., Zhu, M., 2021. The tempo of Ediacaran evolution. Sci. Adv. 7, eabi9643. https://doi.org/10.1126/sciadv.abi9643.
- Yuan, X., Chen, Z., Xiao, S., Zhou, C., Hua, H., 2011. An early Ediacaran assemblage of macroscopic and morphologically differentiated eukaryotes. Nature 470, 390–393. https://doi.org/10.1038/nature09810.
- Zhang, Y., Yang, T., Hohl, S.V., Zhu, B., He, T., Pan, W., Chen, Y., Yao, X., Jiang, S., 2020. Seawater carbon and strontium isotope variations through the late Ediacaran to late Cambrian in the Tarim Basin. Precambrian Res. 345, 105769. https://doi.org/10.1016/j.precamres.2020.105769.
- Zhang, Z., Zhu, G., Wu, G., Li, T., Feng, X., Jing, Y., 2022. Carbon isotopic chemostratigraphy of the Ediacaran-Cambrian successions in the northwestern Tarim Craton, NW China: Correlations with Gondwana supercontinent. Glob. Planet. Chang. 208, 103702 https://doi.org/10.1016/j.gloplacha.2021.103702.
- Zhou, M., Luo, T., Huff, W.D., Yang, Z., Zhou, G., Gan, T., Yang, H., Zhang, D., 2018. Timing the termination of the Doushantuo negative carbon isotope excursion:

- evidence from U-Pb ages from the Dengying and Liuchapo formations, South China. Sci. Bull. 63, 1431-1438. https://doi.org/10.1016/j.scib.2018.10.002.
- Zhu, M., Zhang, J., Yang, A., 2007. Integrated Ediacaran (Sinian) chronostratigraphy of South China. From Snowball Earth to the Cambrian bioradiation: calibration of Ediacaran-Cambrian history in South China. Palaeogeogr. Palaeoclimatol. Palaeoecol. 254, 7–61. https://doi.org/10.1016/j.palaeo.2007.03.025.
- Zhu, W., Zheng, B., Shu, L., Ma, D., Wu, H., Li, Y., Huang, W., Yu, J., 2011. Neoproterozoic tectonic evolution of the Precambrian Aksu blueschist terrane,
- northwestern Tarim, China: Insights from LA-ICP-MS zircon U–Pb ages and geochemical data. Precambrian Res. 185, 215–230. https://doi.org/10.1016/j.precamres.2011.01.012.
- Zhu, M., Lu, M., Zhang, J., Zhao, F., Li, G., Aihua, Y., Zhao, X., Zhao, M., 2013. Carbon isotope chemostratigraphy and sedimentary facies evolution of the Ediacaran Doushantuo Formation in western Hubei, South China. In: Precambrian Research, Biogeochemical Changes Across the Ediacaran-Cambrian transition in South China, 225, pp. 7–28. https://doi.org/10.1016/j.precamres.2011.07.019.